

1N34
53176
3.49

Thermal Modeling With Solid/Liquid Phase Change of the Thermal Energy Storage Experiment

J. Raymond Lee Skarda
Lewis Research Center
Cleveland, Ohio

(NASA-TM-103770) THERMAL MODELING WITH
SOLID/LIQUID PHASE CHANGE OF THE THERMAL
ENERGY STORAGE EXPERIMENT (NASA) 49 p

CSCS 200

N92-13402

Unclas

G3/34 0053176

November 1991

NASA

Thermal Modeling With Solid/Liquid Phase Change of the Thermal Energy Storage Experiment

by

J. Raymond Lee Skarda
National Aeronautics and Space Administration
Lewis Research Center
Cleveland, Ohio 44135

**ORIGINAL CONTAINS
COLOR ILLUSTRATIONS**

Contents

Summary	1
Introduction	1
Symbols	2
Thermal Model Description	3
Model Geometry and Thermal Properties	3
Phase Change Procedure and Logic	7
Simulation of Combined Heating and Cooling Cycles	14
Thermal Model Simulations	14
Results and Discussion	16
Concluding Remarks	19
Appendix A – Finite Difference Solutions and Development of Phase Change Initiation Logic	21
Appendix B – Transient Temperature Profiles For Selected TES Components and Nodes	23
Appendix C – Temperature Contour Plots	41
References	45

Summary

A thermal model which simulates combined conduction and phase change characteristics of thermal energy storage (TES) material is presented. Both the model and results are provided herein for the purpose of benchmarking the conduction and phase change capabilities of recently developed and unvalidated microgravity TES computer programs.

The model was originally developed to support the design and analysis of the NASA Lewis Research Center TES experiment. This report also serves as the preliminary documentation of the thermal models constructed for this experimental effort. The phase change approach developed for the model can be applied to most commercial thermal analyzers and also can be used for other phase change applications. It is again emphasized that the principal intent of this report is to present a model and results for evaluating (benchmarking) computer codes that have been recently developed to predict the behavior of phase change materials in a microgravity environment.

Specifically, operation of the TES-1 experiment is simulated. The heart of the TES-1 experiment is the TES specimen. The specimen is mounted in an approved shuttle payload container known as a Get-Away-Special (GAS), which is also included in the model. The TES specimen consists of the torus shaped TES canister which contains the phase change material (PCM), the conductor rod, and the radiator flare. A heater radiates heat to the outer radius of the TES canister during melting of the PCM. After the lithium fluoride PCM is completely melted, the heater is turned off and latent heat is transferred from the PCM to the conductor rod at the TES canister inner radius. The removed heat is radiated to the environment from the TES radiator flare during solidification. A series of five melting/freezing cycles are simulated.

A two-dimensional SINDA85 model of the TES experiment in cylindrical coordinates was constructed. The phase change model accounts for latent heat stored in, or released from, a node undergoing melting and freezing. However, the volume change of the LiF during the phase change process is neglected. Other phenomena not considered in the model include buoyancy driven and Marangoni flows and the semitransparent behavior of the lithium fluoride (LiF).

Three types of results provided for comparison with other models are transient temperature profiles, color temperature contour plots, and tabulated results. Tabulated results are peak temperatures, freezing times, melting times, and heat losses following each freeze and thaw period. Results from four simulations are presented. Three simulations were performed to investigate the effects of the GAS lid mass on the melting and freezing times of the PCM. The fourth simulation uses a simple approximation to account for combined radiation and conduction transport through the liquid LiF (the semitransparent nature of the solid phase was not included). Results from the lid mass comparison indicate negligible effect on the freezing and melting times for GAS lid masses from 9.1 to 34.1 kg. The semitransparent approximation resulted in decreases of 3.9 percent in freezing times, 3.8 percent in melting times, and 20 K in peak canister temperatures with respect to conduction only.

Introduction

Thermal energy storage (TES) is an attractive technology for solar dynamic power systems proposed for space applications. A TES system would deliver a near-constant temperature working fluid to the turbine during a sun-shade orbit. A typical solar dynamic power cycle which includes the TES material, lithium fluoride (LiF), is shown in figure 1. Energy from the concentrator is stored as latent heat in the LiF. One proposed receiver design utilizing thermal energy storage is illustrated in figure 2. The TES material or phase change material (PCM), is actually contained in small (1.27- to 2.54-cm long) torus shaped canisters that surround the heat pipe. A principal feature of this configuration is that heat (solar flux) is input to the TES material from the outer TES canister radius, while heat is extracted by the heat pipe at the inner canister radius.

Various fluoride salts (e.g., LiF, LiF-CaF₂, NaF) which undergo phase change in the temperature range required for the proposed power cycle have been identified as candidate thermal energy storage materials (ref. 1). However, fluoride salts exhibit as much as a 30 percent change in volume during the phase change process. This leads to the formation of voids during the solidification process. Two concerns which emerge as a

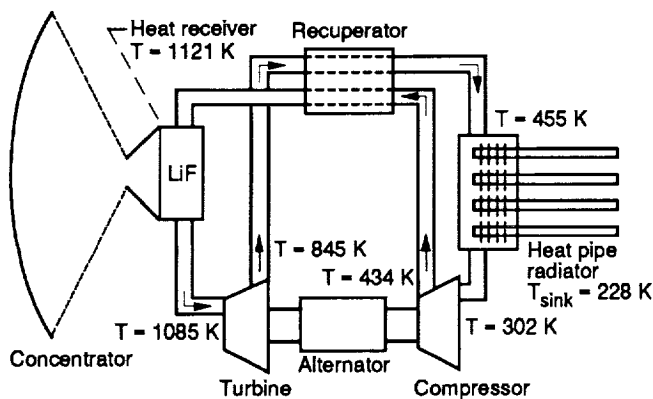


Figure 1.—Typical solar dynamic power cycle.

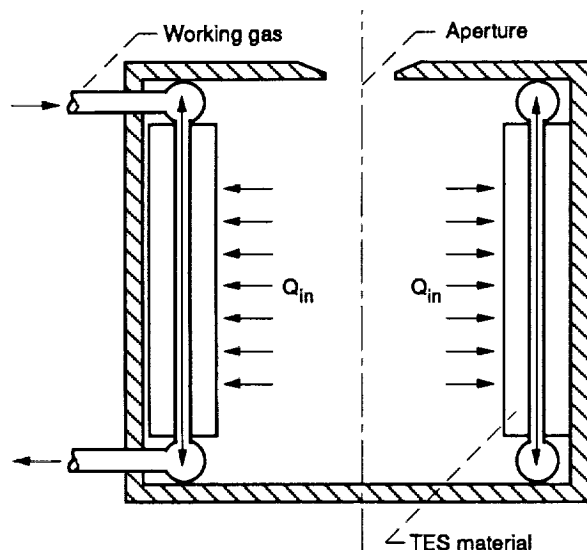


Figure 2.—Typical receiver configuration.

result of void formation are the potential for "ratcheting" of the TES containment wall and development of "hot spots" on the TES canister (containment). Ratcheting is the distortion that occurs if the liquid PCM is unable to expand into the void and instead creates stresses on the canister wall as the PCM continues to liquify during the melting process. Hot spots occur on the canister wall in regions where voids exist between the wall and salt. The present lack of understanding of the freeze-thaw process in a microgravity environment coupled with large volume changes results in conservatively designed TES/receiver systems (refs. 1 and 2). The prediction of void behavior is also of interest to other space related efforts such as possible SP-100 cold restarts.

Computer capabilities to predict void nucleation, movement, and final location/shape in a microgravity environment are being developed (refs. 2 to 4). The computer programs or models must obviously be evaluated to establish their credibility. Confidence in the model is initially established by verification with known

analytical solutions. Additional capabilities can be assessed by benchmarking the unvalidated computer program with a validated computer program. The validated model does not necessarily provide an evaluation (benchmark) of all capabilities of the unvalidated model; thus, it can be less sophisticated than the unvalidated model. The final step in the evaluation process is the validation of the code with actual experimental data.

Microgravity data to validate the microgravity TES models are currently nonexistent. However, a set of space flight experiments, the NASA Lewis TES flight experiments, are presently being designed and constructed to provide both insight into the void behavior and the data to evaluate these computer models (ref. 1). In support of the TES experimental design effort, thermal analysis has been performed that can also be used in the evaluation (benchmarking) of the microgravity TES computer programs. The model and results from this analysis are presented for the purpose of benchmarking some of the capabilities of the unvalidated TES computer models.

Combined conduction and phase change within the phase change material (PCM) are simulated in the model presented. The PCM volume change during phase change is not simulated. Since the model was originally constructed for design and analysis purposes, the assumptions and modeling approach were strongly influenced by design considerations. However, the emphasis of this report is on presenting sufficient information for comparison with results from other models or computer programs.

Symbols

C	thermal capacitance J/K
C_p	specific heat, J/kg-K
G_{ij}	linear conductance between the i and j nodes
G_{rad}	radiation conductance between the i and j nodes
h	contact conductance, W/m ² -K
h_{lat}	latent heat, J/kg
K	thermal conductivity, W/m-K
k	counter - k th iteration
m_i	mass of i th node, kg
N	number of nodes

Q_{ERR}	convergence limit for phase change initiation or completion logic
$Q_{exs,i}$	excess latent heat of i th node at phase change completion time step
$Q_{i,lat}$	cumulative latent heat of the i th node
$T_{i,n}$	temperature of the i th node at time n
$T_{j,n}$	temperature of the j th node at time n
T_{lat}	solid/liquid phase change temperature, K
t_n	discrete time value immediately prior to phase change completion
t_{n+1}	discrete time value immediately following phase change completion
X_i	liquid mass fraction
Δt	time step
$m\Delta t_{m+1}$	time step in which phase change initiation occurs
$n\Delta t_{n+1}$	time step in which phase change completion occurs
ϵ	emissivity
ϵ_{eff}	effective multilayer insulation (MLI) emissivity
η	latent heat content error
Subscripts:	
i	i th node
os	overshoot
r	radiation conductors

Thermal Model Description

Reasonably complete descriptions of the model geometry, model properties, phase change logic, orbit simulation, and general modeling approach are provided in this section. A familiarity with the modeling approach and assumptions are important for the correct interpretation of the model results. In addition, an understanding of all the above items is critical for comparison of model

results to other numerical or predicted results. Finally, a detailed discussion of the phase change approach is provided because the logic can easily be incorporated into other thermal models with different phase change applications.

Model Geometry and Thermal Properties

The thermal model geometry of the proposed TES design was constructed with the use of PATRAN. The PATRAN model was then converted to a SINDA model in cylindrical coordinates. Since PATRAN is a finite element computer program while SINDA is a lumped parameter (lumped volume) computer program, PATRAN nodes and SINDA nodes are not equivalent. The term "node" in this report shall always imply a SINDA node unless otherwise stated. The node diagrams for the overall model and TES specimen are shown in figures 3 and 5, respectively, while dimensions for the overall model and TES specimen are found in figures 4 and 6, respectively. The model is two-dimensional in the radial and axial directions and is comprised of 127 nodes.

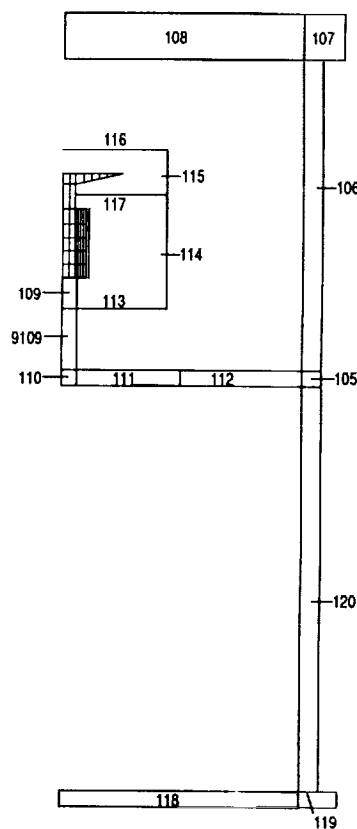


Figure 3.—GAS/TES node diagram.

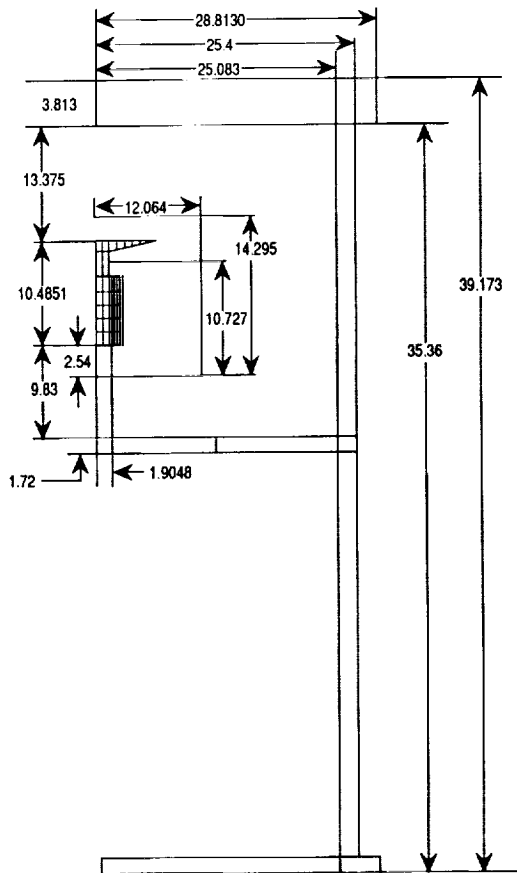


Figure 4.—GAS/TES model dimensions (cm).

Node distribution is as follows:

TES specimen nodes	108
LiF nodes	20
MLI	5
Lid, GAS, and support structure	12

The node distribution reflects the level of detail that was used in representing various components. Hence, from the above node distribution, we observe a relatively detailed TES specimen model, while the GAS walls, GAS lid, and MLI are coarsely represented. When attempting to compare the results with other numerical analyses, it is also helpful to give a breakdown of diffusion nodes, arithmetic nodes, and boundary nodes. Diffusion nodes are nodes with finite capacitance values (i.e., time varying nodes), while arithmetic nodes have zero capacitances (also referred to as massless nodes). Rigorously, the temperature of an arithmetic node at each time step is simply the thermal conductance weighted average temperature of all nodes in contact with the given node. Boundary nodes are nodes with constant temperatures. The distribution of diffusion, arithmetic, and boundary nodes in the thermal model is, 70, 55, and 2, respectively. Most, but not all,

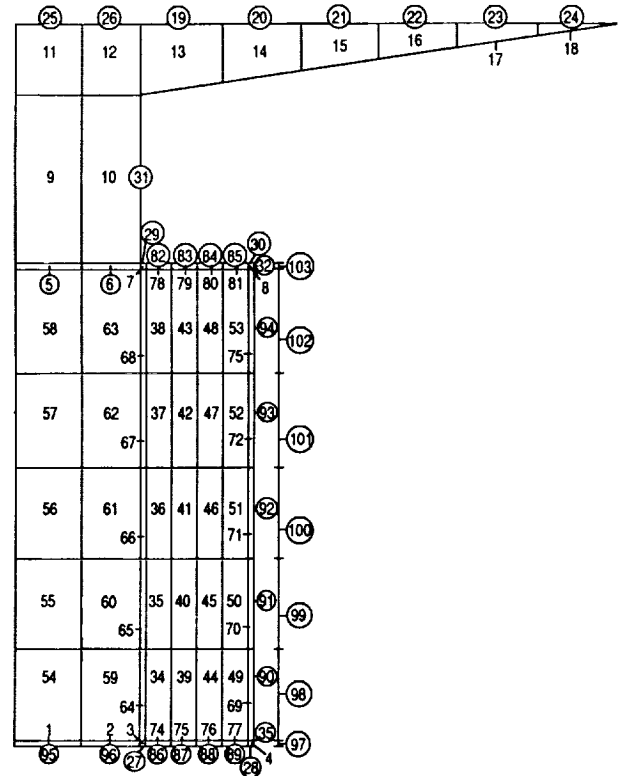


Figure 5.—TES specimen node diagram. Circles denote arithmetic nodes.

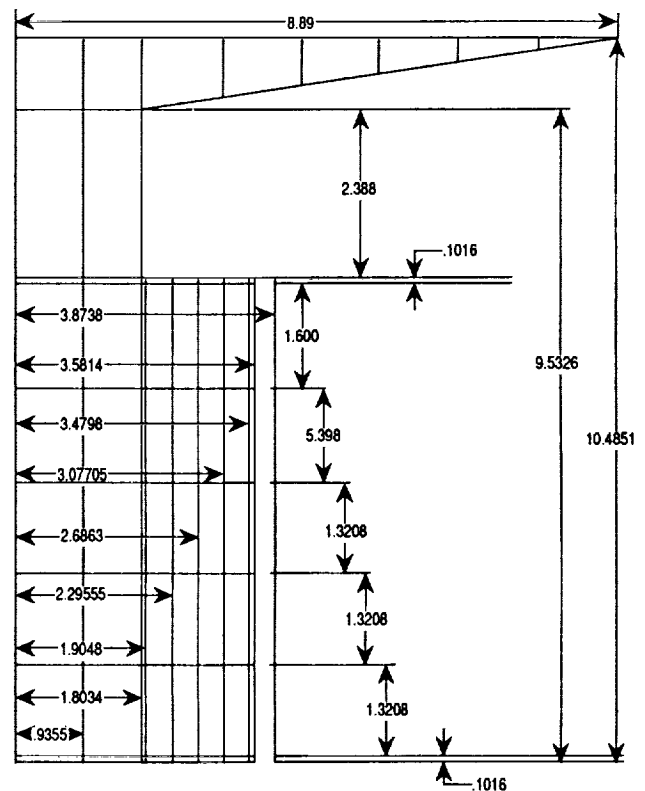


Figure 6.—TES specimen dimensions (cm).

of the linear conductances were generated from the PATRAN model, while radiation conductances were computed with the use of TRASYS and then were incorporated into the SINDA thermal model. The numbers of linear, nonlinear (radiation), and total conductances are 932, 202, and 1134, respectively.

The TES specimen is mounted in an approved shuttle payload container previously known as a Get-Away-Special (GAS) and more recently designated as a Complex Autonomous Payload (CAP). The GAS (or CAP) is a cylindrical aluminum container with an internal diameter and length (user length) of 0.5017 and 0.7176 m, respectively. In figure 7, the TES specimen is shown mounted in the upper portion of the GAS. The battery and electronics will be located in the region below the

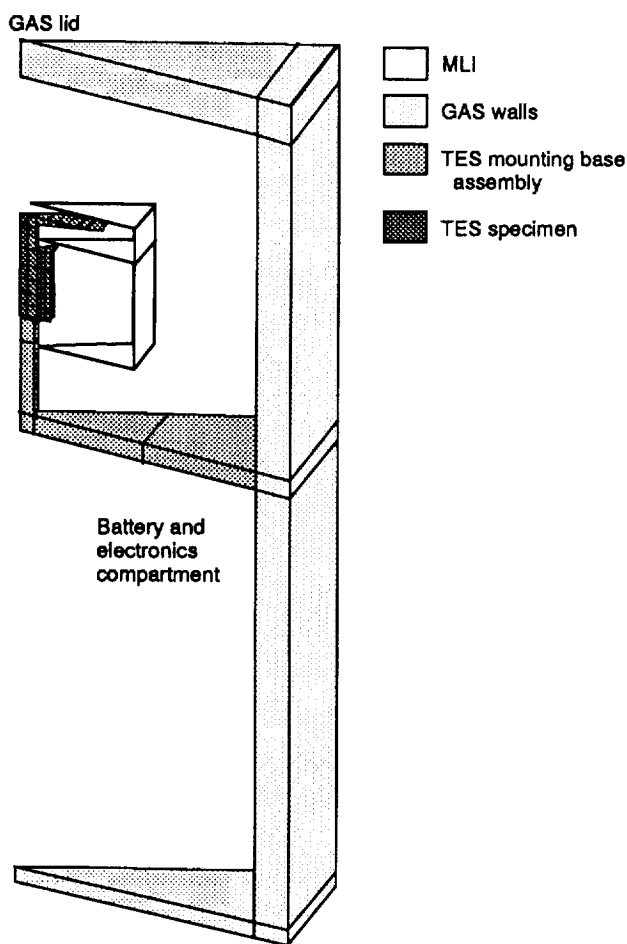


Figure 7.—TES/GAS configuration.

TES specimen. The surrounding MLI and mounting base assembly thermally isolates the TES specimen from the battery and electronics compartment and the GAS walls. The mounting base assembly consists of two silica spacers, four Haynes-188 bolts, and the molybdenum heater bracket, which is sandwiched between the spacers. As illustrated in the GAS/TES node diagram (fig. 3), the Haynes-188 mounting bolts and silica spacer

are combined. The thermal capacitances of the four bolts and silica spacer are summed together to obtain capacitances of the mounting base nodes, nodes 109 and 9109. Thermal conductances of the mounting base nodes were computed by assuming parallel conductances (resistances) between the bolts and the spacer. The axial thermal resistance of the thin molybdenum heater bracket is negligible relative to the spacer thermal resistance. However, on each side of the heater bracket a contact conductance, h , of 400 W/m-K was included in the thermal model.

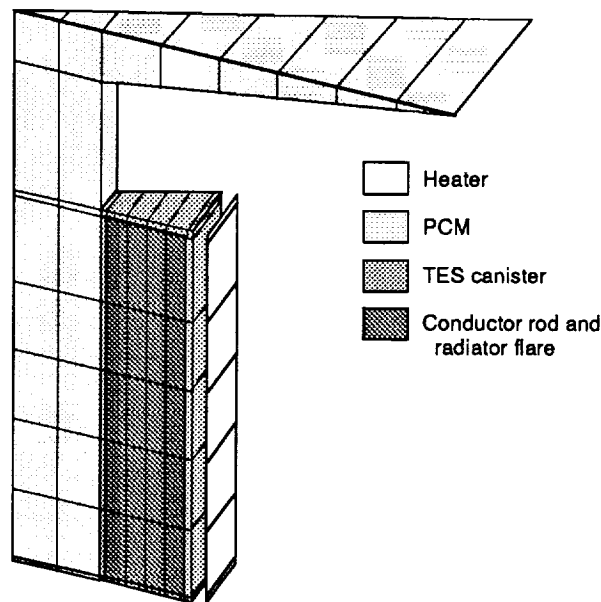


Figure 8.—TES specimen.

An enlarged view of the TES specimen is shown in figure 8. The conductor rod, radiator flare, and the TES canister are made of Haynes-188 alloy. For this configuration, the heat is radiated from the heater to the TES canister. Heat is transferred from the heater in the following ways: radiated to the canister wall, radiated through the upper and lower gaps between the canister wall and heater, and radiated from the heater to the MLI. Conduction from the heater along the heater mounting bracket is not included in the model. However, the model is flexible enough to allow a bracket to be included in subsequent analyses. For assembly purposes, the radiator flare is detachable from the conductor rod. Therefore, a radiator flare/conductor rod contact conductance of 400 W/m-K is also included in the model. While the MLI that surrounds the TES specimen is fixed, the MLI blanket, or cover, above the radiator flare is movable. A shutter mechanism is used to open the blanket and expose the radiator flare to the GAS lid during the solidification (cooling) portion of the cycle. During the melting (heating) portion of a cycle, the MLI cover is closed to insulate the radiator surface

from the surrounding environment. The simulation of the alternating heating and cooling portions of the orbital cycles is discussed later. A total heater power of 260 watts, or a heat flux of 15.1 kW/m^2 , was applied to the heater during the melting portion of each cycle. In each simulation, power was applied until all the PCM was melted.

The thermophysical properties used in the model are summarized in tables I to IV. Temperature dependent specific heats and thermal conductivities associated with the model materials and components are given in table I.

Constant values of densities and latent heat of fusion are shown in table II. Emissivities of various surfaces that were used to calculate radiation conductor values are given in table III. Contact conductances are given in table IV. Contact conductive values were chosen from a range of values provided in reference 6.

The spacer thermal conductance values shown in table I refer to the mounting base spacer below the TES specimen, as indicated in figure 7. The spacer thermal conductances were computed by assuming the thermal

TABLE I.—TEMPERATURE DEPENDENT PROPERTIES

[Specific heat, Cp, thermal conductivity, K, thermal conductance, U.]

Specific heat for Haynes 188 alloy ^a							
Temperature, K	273	673	873	1073	1273	1473	
Specific heat, J/kg-K	398	486	523	557	590	624	
Thermal conductivity for Haynes 188 alloy ^a							
Temperature, K	311	644	811	1033	1200	1477	
Thermal conductivity, W/M-K	10.8	17.0	19.9	24.1	25.8	30.5	
Specific heat for LiF ^b							
Temperature, K	500	1121.3	1121.4	1500			
Specific heat, J/kg-K	1631	1631	2453	2453			
Thermal conductivity for LiF ^b							
Temperature, K	500	600	800	1000	1121.2	1121.3	1500
Specific heat, J/kg-K	8.08	6.61	5.61	5.98	6.34	1.73	1.73
Specific heat for aluminum (from ref. 5)							
Temperature, K	200	250	300	400	500		
Specific heat, J/kg-K	797	859	902	949	997		
Thermal conductivity for aluminum (from ref. 5)							
Temperature, K	200	250	300	400	500		
Thermal conductivity, W/M-K	237	235	237	240	236		
Thermal conductance for spacer (Node 109)							
Temperature, K	311	811	1033	1477			
Thermal conductance, U, W/K	0.01376	0.02133	0.02482	0.03014			

^aProperty values obtained from Haynes Alloy No. 188 Manufacturer Physical Property Brochure, Haynes International Inc., Kokomo, IN.

^bProperty values obtained from Hitchhiker Shuttle Payload of Opportunity Carrier Customer Accommodations and Requirements Specifications. HHG-730-1503-05 (draft copy 2/90), NASA Goddard Space Flight Center, Greenbelt, MD.

TABLE II.—CONSTANT PROPERTIES

Density, kg/m ³	
Haynes 188	8980
LiF	1690.3
Al at 300K (from ref. 5)	2701
LiF latent heat, kJ/kg	1037

TABLE III.—MODEL EMISSIVITIES

Component	Emissivity
GAS lid outer surface	0.75
Gas lid inner surface	.75
GAS wall inner surface	.75
GAS wall outer surface	.75
MLI inner surface	.10
MLI effective emissivity	.0025
PCM void	.5
TES canister wall	.7
Heater inner surface	.55
Heater outer backing	.5
Radiator flare top	.5
Radiator underside	.5
Conductor rod neck	.5

TABLE IV.—MODEL CONTACT
CONDUCTANCES

Interface	Conductance, h , W/m^2-K
Radiator flare to conductor rod	400
Spacer to heater bracket	1200

resistance of the four Haynes-188 bolts and the ceramic spacer to be in parallel. The thermal capacitance of the ceramic spacer relative to that of the bolts was neglected. Therefore, the total spacer thermal capacitance is the sum of the four bolt thermal capacitances.

As depicted in figure 7, the MLI blanket that surrounds the TES specimen is represented by a series of arithmetic nodes. The inner surface, facing the TES specimen, is given an emissivity ($\epsilon = 0.1$) typical of an MLI foil surface. An "effective" emissivity, ϵ_{eff} , represents the radiative resistance of the MLI nodes. The effective emissivity value is chosen to yield a desired or acceptable average heat loss through the MLI during a complete melting of the PCM. For example, the ϵ_{eff} of 0.0025 given in table III yields an acceptable MLI average heat loss of -52 W during PCM melting. Determination of the appropriate ϵ_{eff} is an iterative procedure of guessing ϵ_{eff} , running the melt/freeze simulation, and adjusting the new guess of ϵ_{eff} based on prior MLI heat loss prediction.

Most of the heat rejected during the TES experiment is radiated to the GAS lid. The lid is considered to be in excellent thermal contact with the rest of the GAS canister. Therefore, to minimize the temperature rise in both the lid and canister, it is necessary to reject as much heat as possible to the environment. According to a draft GAS requirements document,¹ various options are available for heat rejection from the GAS canisters. One such option calls for painting the outside surfaces of the GAS canister white to obtain an emissivity of 0.86. Another option may be to paint the inside surfaces of the GAS canister to obtain emissivities of approximately 0.8. As indicated in table III, a conservative emissivity value of 0.75 was applied to all GAS surfaces in the present thermal model. If GAS emissivities greater than 0.75 are obtained, then the heat rejection capability will improve.

Phase Change Procedure and Logic

The phase change modeling approach is described here in detail because this approach is different from

the standard approach, which uses the effective specific heat Cp_{eff} (ref. 7), that can be applied to most thermal analyzers. One objective of the model is to provide results that will be used to benchmark computer codes currently being developed to predict the behavior of PCM (refs. 2 to 4). Therefore, a thorough understanding of the actual capabilities and limitations of the phase change logic is necessary to determine which characteristics of the unvalidated computer program are actually being benchmarked. The following discussion details the latent heat simulation and the initiation and completion of the phase change logic. The development of the latent heat simulation (phase change) logic is described in appendix A.

The present phase change model accounts for latent heat stored in, or released from, a node undergoing melting and freezing. The phase change model correctly accounts for latent heat as part of the nodal energy balance. However, other phenomena associated with the phase change of PCM's are not considered. The model does not account for the volume change of the LiF during the phase change process. Buoyancy driven and Marangoni flows during the liquid phase are also not considered. Specifically, general conduction and solid-liquid phase change predictions from other computer codes can be benchmarked.

Most commercial thermal analyzers do not explicitly include a latent heat term as part of the energy equation algorithm. However, as described below, it is relatively easy to add the capability of simulating nodal latent heat change. The most common approach is to increase the thermal capacitance of a node so that the sensible heat, $Cp_{eff}\Delta T_{lat}$, over the temperature interval defined by ΔT_{lat} is equal to h_{lat} (ref. 7). Thermal analyzers that provide access to the basic solution variables (i.e., nodal temperature, thermal capacitance, and thermal conductance) allow a slightly different approach which is numerically simpler and more robust. This more robust approach has been incorporated into the current model. The major difference between the two approaches is that the infamous "machine roundoff error," the chief disadvantage of the more common approach that uses effective specific heat Cp_{eff} (ref. 7), is used advantageously to maintain a constant nodal phase change temperature in the current approach. In addition, a constant phase change temperature is not possible in the effective Cp approach; rather, a small phase change ΔT is necessary (ref. 8).

When phase change is initiated, the node thermal capacitance, C_i , is set equal to a very large value (e.g., 10^{25}). A sufficiently large C_i value results in an extremely small temperature change that is rounded off by the machine to zero. Therefore, the node temperature remains constant. Simulation of phase change is accomplished by cumulatively summing the net heat

¹Hitchhiker Shuttle Payload of Opportunity Carrier Customer Accommodations and Requirements Specifications. HHG-730-1503-05. (Draft copy 2/90), NASA Goddard Space Flight Center, Greenbelt, MD, pp. 2-44.

flow into the node at each time step as given by equation (1).

$$Q_{i,lat} = Q_{i,lat} + \sum_{j=1}^N \left[G_{ji} (T_{j,n} - T_{i,n}) + G_{rad} (T_{j,n}^4 - T_{i,n}^4) \right] \Delta t \quad (1)$$

During a melting process and a solidification process, the liquid mass fraction of the i th phase change node is computed from equations (2) and (3), respectively.

$$X_i = \frac{Q_{i,lat}}{m_i h_{lat}} \quad (\text{melting}) \quad (2)$$

$$X_i = 1 - \frac{Q_{i,lat}}{m_i h_{lat}} \quad (\text{freezing}) \quad (3)$$

When sufficient heat is accumulated or lost to completely melt or solidify the node, then the liquid mass fraction, X_i , is equal to 1 or 0, respectively. The phase change process is then terminated by computing the appropriate value of C_i required for sensible heat process.

The explicit steps used to simulate melting and solidification for the present analysis are presented in the flowchart illustrations, figures 9 and 10, respectively. The primary function of this logic is to maintain

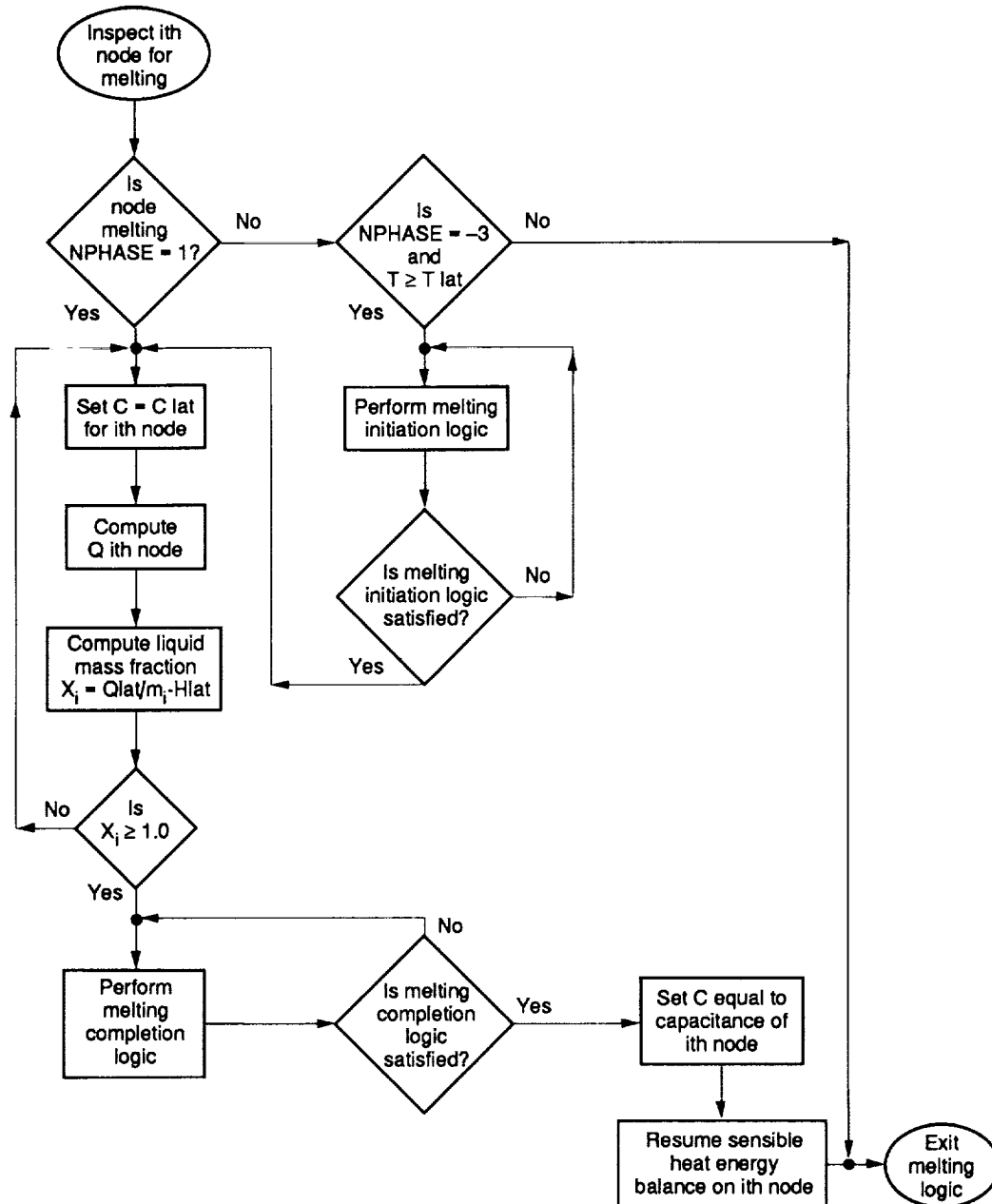


Figure 9.—Melting logic.

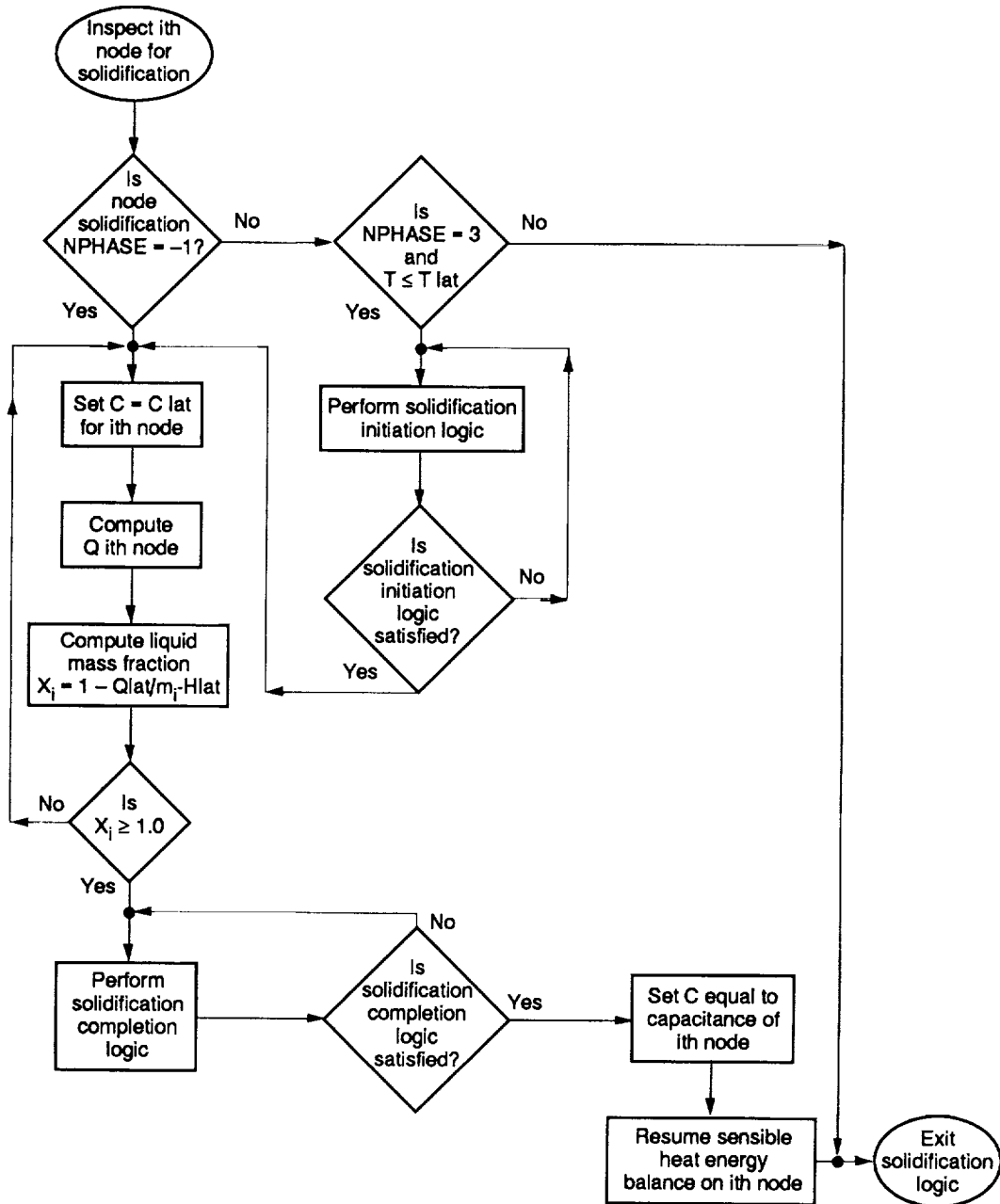


Figure 10.—Solidification logic.

the temperature constant and compute the liquid mass fraction during phase change. In addition, the state of the phase change nodes and the direction of phase change are tracked through the use of the flag, NPHASE. This is actually an array in the model that contains an element for each phase change node. For a given node, NPHASE values of 1, -1, 2, -2, 3, and 3, -3 indicate that the node is melting, solidifying, initiating completion of melting, initiating completion of solidification, liquid, and solid, respectively. The flowchart boxes in figures 9 and 10 that identify the initiation or completion of phase change are expanded in figures 11 to 14.

The question of when to apply the phase change logic must now be addressed. Since each time step, Δt , is finite, the probability is low that the temperature T_i will be exactly equal to T_{lat} at a given discrete time, t_m . The discrete times that bound the unknown time at which melting of the i th node begins, t_{lat} , are denoted as t_m and t_{m+1} , while the time step between t_m and t_{m+1} is defined as Δt_{m+1} . For melting, the times, t_m and t_{m+1} can be determined by satisfying the criteria $T_{i,m} < T_{lat}$ and $T_{i,m+1} > T_{lat}$. For solidification, the above inequality signs are reversed. Therefore, the fundamental criterion that is used to identify when phase

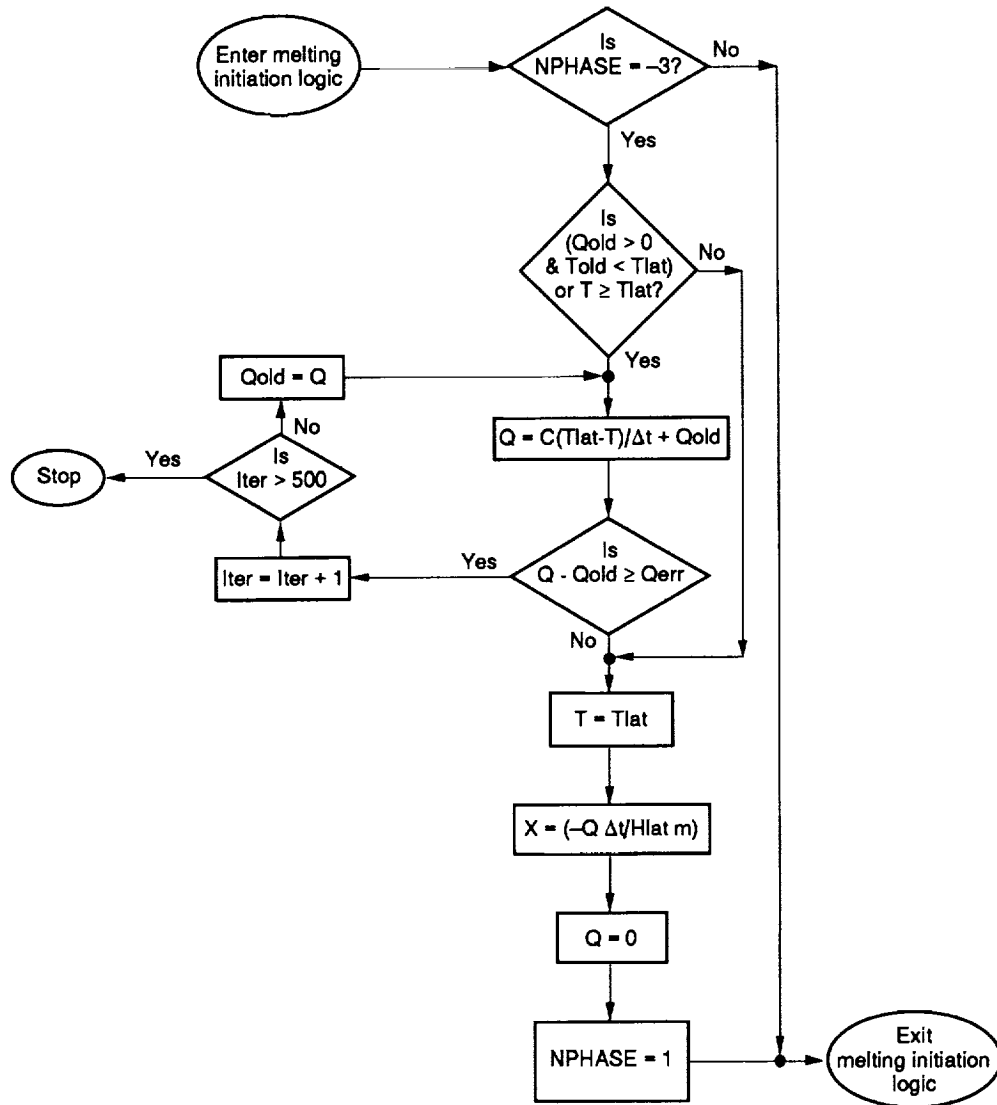


Figure 11.—Melting initiation logic.

change should begin is when the temperature difference $(T_{i,m} - T_{lat})$ changes sign from $(T_{i,m+1} - T_{lat})$. If the temperature difference (overshoot) between T_{m+1} and T_{lat} is small, then the sensible heat overshoot, $Q_{i,os}$, is negligible, and $t_{m+1} \equiv t_{lat}$ and $T_{i,m+1} \equiv T_{lat}$.

$$Q_{i,os} = \frac{C_i}{m \Delta t_{m+1}} (T_{i,m+1} - T_{lat}) \quad (4)$$

The simplest approach to correct for non-negligible values of $Q_{i,os}$ is to repeat the simulation using a smaller time step. When a limited number of simulations are required, this may prove to be the quickest approach. Disadvantages of this method are the increase in simulation time for the reduced time step and the additional number of simulations. An alternative is to develop a method that computes the initial latent heat change of the i th phase change node during the $m \Delta t_{m+1}$ time step. If the finite difference solution is explicit in

time, then the latent heat contribution, $Q_{i,lat}$, during the $m \Delta t_{m+1}$ time step is simply equal to $Q_{i,os}$. As described in appendix A, no iteration is required for an explicit solution routine. However, in fully implicit or implicit/explicit (e.g., Crank-Nicholson) finite difference solutions, all node temperatures are solved for simultaneously at each given time, say t_{m+1} . Therefore, the latent heat contribution during the $m \Delta t_{m+1}$ time step must be determined iteratively for implicit or implicit/explicit solution routines.

An iterative scheme was devised that corrects for the temperature overshoot by computing the latent heat contribution during the time step that phase change was initiated, $m \Delta t_{m+1}$. For illustration purposes, a simple implicit finite difference energy equation which includes a heat source term, Q_i , is given by equation (5). The heat source term, Q_i , is treated as a latent heat term during the $m \Delta t_{m+1}$ time step for the i th node. The

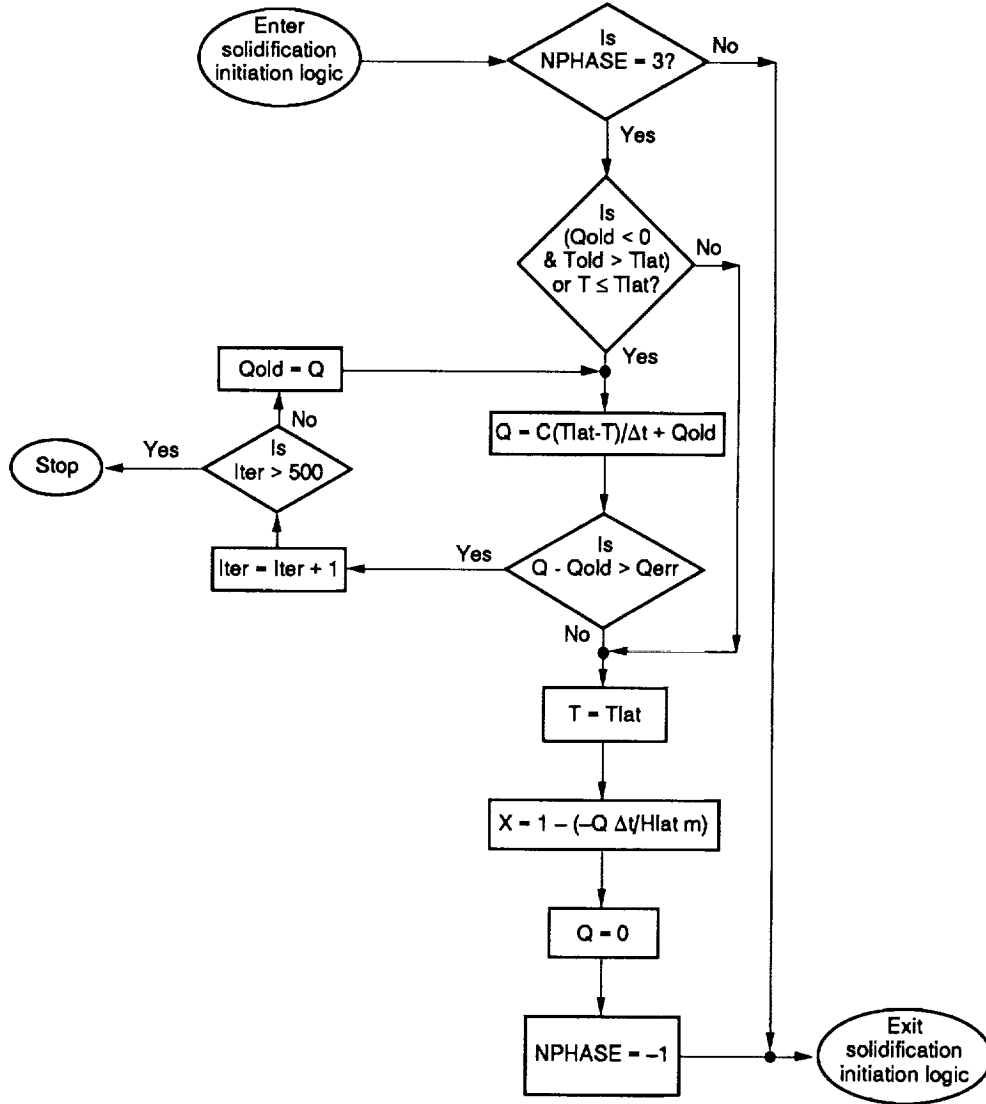


Figure 12.—Solidification initiation logic.

superscript k 's represent the iteration during computation of latent heat contribution over the $m\Delta t_{m+1}$ time step. An initial guess ($k=0$) of $T_{i,m+1}$ is computed from the solution routine such as equation (5). During the initial ($k=0$) estimate of $T_{i,m+1}$, the source term, Q_i is equal to zero. A heat source term for the next ($k+1$) iteration, $^{k+1}Q_i$, is computed from equation (6) by using the $^kT_{i,m+1}$ value calculated from equation (5). If the convergence criterion, equation (7), is not satisfied, the $^{k+1}Q_i$ is used in the subsequent iteration to compute the new ($k+1$) estimate of $T_{i,m+1}$. The convergence of Q_i correctly requires $T_{i,m+1} \rightarrow T_{lat}$, which is observed in equation (6). After equation (7) has been satisfied, the initial latent heat contribution, $Q_{i,lat}$, is set equal to Q_i . The initial liquid mass fraction at $t=t_{m+1}$ is then computed by using equation (2) or (3).

$$^kT_{i,m+1} = T_{i,m} + \frac{\Delta t}{C_i \left[^kQ_i + \sum_{j=1}^N G_{j,i} \left(^kT_{j,m+1} - ^kT_{i,m+1} \right) \right]} \quad (5)$$

$$^{k+1}Q_i = \frac{C_i (T_{lat} - ^kT_{i,m+1})}{\Delta t} + ^kQ_i \quad (6)$$

$$\left| ^{k+1}Q_{i,os} - ^kQ_{i,os} \right| < QERR \quad (7)$$

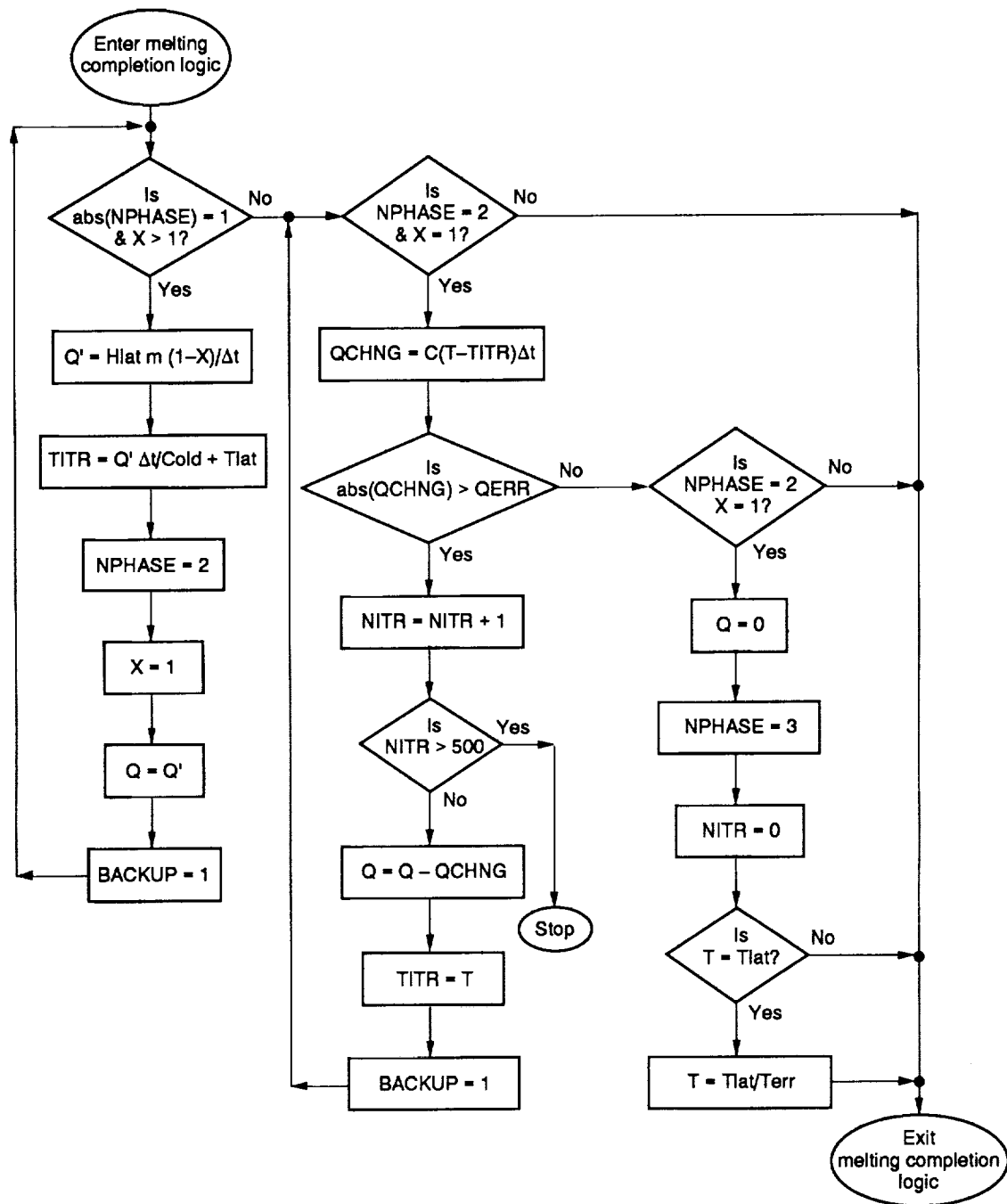


Figure 13.—Melting completion logic.

The iterative scheme to initiate melting of a given i th node was implemented in the thermal model by using the overall approach diagrammed in figure 11. Similarly, the logic that was developed to initiate solidification is shown in figure 12. The actual variable names used in the model are also used in the flowcharts (figs. 9 to 14). The flowchart variable names T , T_{old} , Q , and Q_{old} in figures 11 and 12 correspond to $T_{i,m+1}$, $T_{i,m}$, $^{k+1}Q_i$, and kQ_i . When the flag $NPHASE$ is equal to -3 or 3, initiation of melting or freezing occurs, and the iterative scheme described above is

executed. Iteration limits are also observed in figures 11 and 12. If the convergence criteria are not satisfied after 500 iterations, the simulation is stopped and a diagnostic message is written to the log file.

Criteria must be provided to determine when phase change of the i th node is completed. Similar to the phase change initiation problem, the heat transferred to the node results in both latent and sensible heating during the ${}_n\Delta t_{n+1}$ time step. Analogous to the initiation of phase change case, an iterative scheme is again developed. The objective, however, is to determine the

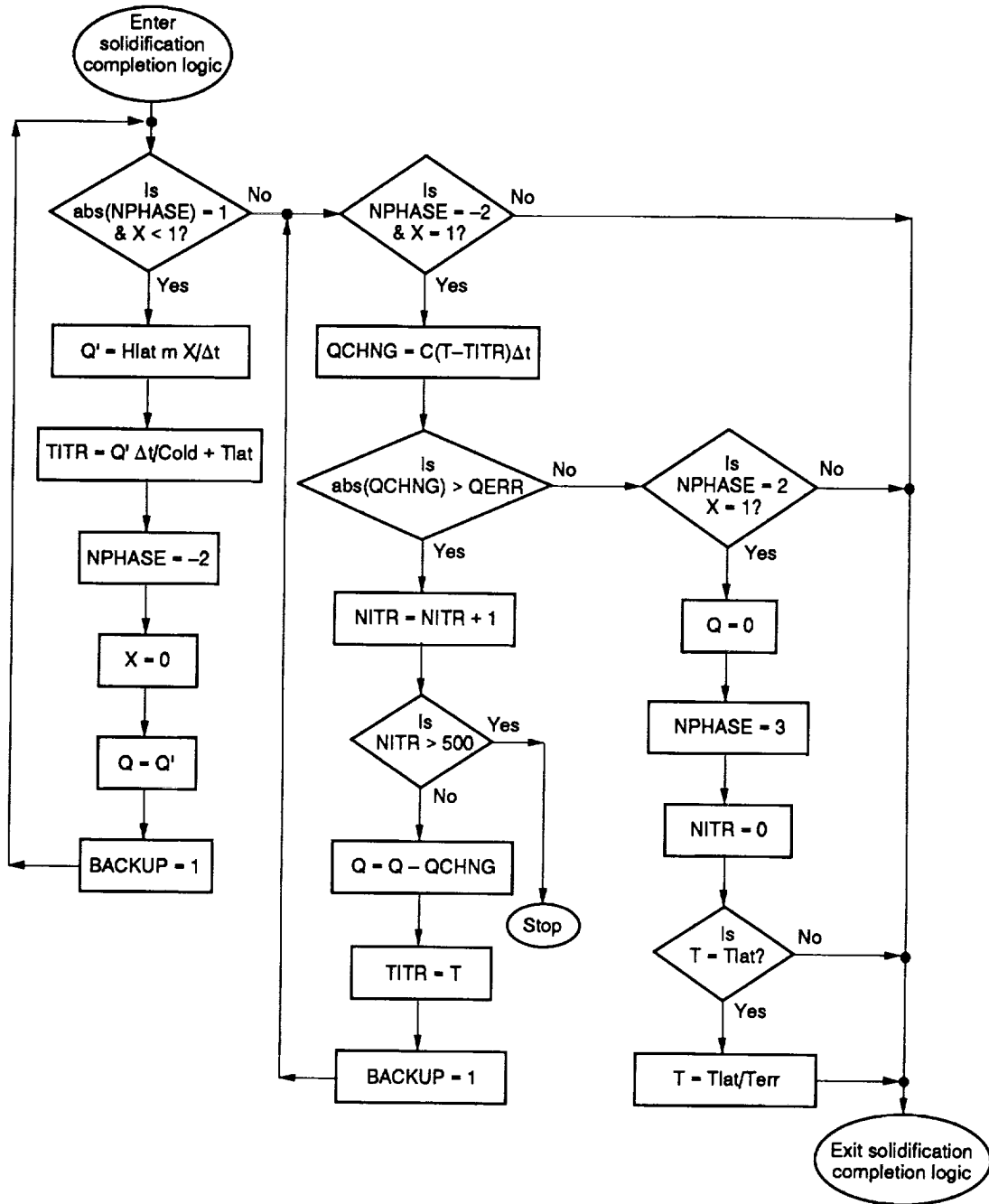


Figure 14.—Solidification completion logic.

sensible heat contribution and resulting temperature rise in the $n\Delta t_{n+1}$ time step.

The completion of phase change time step is defined as $n\Delta t_{n+1} = t_{n+1} - t_n$. The times t_n and t_{n+1} are determined by satisfying the criteria given in equation (8) or (9) for melting or solidification, respectively.

$$X_{i,n} < 1 \quad \text{and} \quad X_{i,n+1} > 1 \quad (\text{Melting}) \quad (8)$$

$$X_{i,n} > 0 \quad \text{and} \quad X_{i,n+1} < 0 \quad (\text{Solidification}) \quad (9)$$

The general approach that was used to determine the latent heat contribution during initiation of phase change is used to compute the sensible heat contribution during completion of phase change. The excess latent heat, $Q_{\text{exs},i}$, at the $n\Delta t_{n+1}$ time step is computed from equation (10) or (11). On the initial pass ($k=0$ iteration) through the phase change completion logic, $Q_{\text{exs},i}$ is used to make two guesses of $T_{i,n+1}$. One estimate of $T_{i,n+1}$ is from equation (12). The second estimate is obtained from the solution routine of equation (5), by using Q_{exs} as the heat source term Q_i . The value of

$T_{i,n+1}$ obtained from equation (12) is defined as ${}^{\circ}T_{i,n+1}$, while the $T_{i,n+1}$ value computed from equation (5) is ${}^1T_{n+1}$. A change in the heat source term, ΔQ_i , which is computed from equation (13), is then used to determine the heat source for the next iteration, ${}^{k+1}Q_i$. The phase change completion logic used in the model is shown in figures 13 and 14. The variable names Hlat, m, TITR, Q', QCHNG, Q, and NITR used in both the flowcharts and the model correspond to h_{lat} , m_i , $T_{est,i}$, $Q_{exs,i}$, ΔQ_i , Q_i , and k.

$$Q_{exs,i} = \frac{h_{lat}m_i(1 - X_i)}{\Delta t} \quad (\text{Melting}) \quad (10)$$

$$Q_{exs,i} = \frac{h_{lat}m_i(X_i)}{\Delta t} \quad (\text{Solidification}) \quad (11)$$

$$T_{est,i} = \frac{Q_{exs}\Delta t}{C_i} + T_{lat} \quad (12)$$

$$\Delta Q_i = \frac{C_i \left({}^{k+1}T_{i,n+1} - {}^kT_{i,n+1} \right)}{\Delta t} \quad (13)$$

$${}^{k+1}Q_i = {}^kQ_i - \Delta Q_i \quad (14)$$

$$\Delta Q_i < QERR \quad (15)$$

A QERR value of 1 J/kg was used for the thermal model simulations discussed later. The maximum nodal latent heat content error for the smallest PCM nodes is 0.1 percent, while the maximum error in nodal latent heat content for the largest PCM node is 0.05 percent. The nodal latent heat content error, η , is defined as

$$\eta_i = \frac{QERR}{m_i h_{lat}} \quad (16)$$

Simulation of Combined Heating and Cooling Cycles

Slight differences in model geometry exist between the heating and cooling modes. The differences result from the open and closed positions of the MLI shutter during cooling and heating, respectively. The approach that is used to address the model geometry differences relies heavily on various features of the thermal analyzer, SINDA/FLUINT, that was chosen for the analysis.

Therefore, the terminology and nomenclature used in this section requires some familiarity with SINDA/FLUINT.²

During the melt/freeze cycle simulations, the open and closed positions of the radiation shutter must be modeled to properly simulate cooling and heating portions of the cycles, respectively. The radiator flare radiates directly to the GAS lid during the cooling portion of a cycle, while the radiation shutter is simulated closed for the heating portion of the cycle. The arithmetic node 116 (see figure 5) represents the radiation shutter in the closed position. Two sets of radiation conductances, one for the heating mode (Heating RADK's), and another set for the cooling mode (Cooling RADK's) are generated for the model. For the closed shutter (heating) mode, the Heating RADK's are computed to the outside MLI surfaces (from the MLI to the GAS) and to the inside surfaces (from the TES specimen to the MLI) using two separate TRASYS models. The Cooling RADK's consist of radiation conductors from the TES specimen to the surrounding MLI, radiation flare to the GAS lid, and radiation conductors from the MLI to the GAS.

Both sets of radiation conductances cannot be applied simultaneously. The Cooling RADK's must be "turned off" during the heating mode, while the Heating RADK's must be "turned off" during the cooling mode. Therefore, the actual conductance values of the Cooling RADK's are saved in a dummy array during the heating mode. The Cooling RADK's in the conductance block of the model are then set to zero. During cooling, the actual values of the Cooling RADK's are restored. The conductance values of the Heating RADK's are then transferred to a dummy array and zeroed out during the cooling mode.

The transfer of conductance values to and from the dummy arrays occurs in the operations block. After completion of the melting or freezing criteria in variables 2, TIMEND is set equal to TIMEO. This stops execution of the network solution subroutine (in this case FWDBCK) and returns control to the operations block. By use of a DO LOOP which encloses the network solution subroutine, the melt/freeze cycle scenario can be simulated for a user specified number of orbits.

Thermal Model Simulations

The data presented and discussed herein are intended principally for comparison with other computer programs that have recently been developed to predict the behavior of PCM with large volume changes (refs. 2 to 4). Combined conduction and constant density phase change capabilities of the recently developed computer

²Cullimore, B.A., et al.: SINDA '85/FLUINT User's Manual, Version 2.3. NASA Contract NAS9-17448; MCR-90-512, Martin Marietta Corporation, Denver, CO, 1990.

programs can be benchmarked with these results. This section also serves to document the initial thermal modeling that was performed in support of the TES-1 experiment design effort. The modeling approach was strongly influenced by the need to provide conservative thermal analysis results for design purposes. Predictions of power requirements, peak temperatures, and freezing/melting times were performed as part of the TES-1 conceptual design. Model approximations, assumptions, and limitations that were influenced by design considerations are briefly summarized below.

As indicated in the section titled Phase Change Procedure and Logic, the SINDA thermal model is not capable of predicting the actual phenomena occurring in the TES material. Phenomena which cannot be simulated directly with the thermal model include the translucent behavior of the lithium fluoride, the 30 percent volume change of the salt, and the buoyancy driven and Marangoni flows. Both the lack of required property data and the complexity of the semitransparent behavior require major simplifying assumptions for the present thermal analysis. Void formation also changes the thermal characteristics of the TES canister, because the proportion of heat transfer from the canister wall to the TES material by radiation and conduction changes as the void grows and shrinks. Therefore, conservative assumptions were applied, when possible, that would predict greater total power and higher canister wall temperatures than would actually occur during the experiment.

The following approximations and assumptions should be kept in mind while reviewing the results or comparing them with other data:

(1) Buoyancy driven and Marangoni flows are neglected. Therefore, the thermal resistance of the TES material is greater, and this requires more heating and cooling energy to melt and solidify the TES material, respectively. The canister wall peak temperatures also increase (conservative).

(2) The void is placed in the realistically worse location for heating. The void is expected to migrate to a hot spot. For the TES-1 experiment, this will be at the outer wall. Placing the void along the whole outer canister wall requires that heat be transferred to the TES material by radiation. A small amount of heat is also conducted along the wall and then is conducted from the top and bottom canister walls into the TES material. This assumption increases both the peak canister wall temperature and the energy required to melt the TES material.

(3) Heat losses from thermocouples are not included in the simulation. Conduction losses from the heater through the heater base are also neglected (nonconservative).

The following is a description of the characteristics and scenarios modeled in each of the four simulations

identified in table V. Each simulation is divided into two scenarios—an initial heatup of the TES specimen, and the TES melt/freeze cycles. The initial heatup simulation begins with the initial temperatures of 300 K and continues through complete melting of the PCM. This simulates the start of the actual experiment on board the orbiter. The effects of a prolonged cooldown period prior to initiation of the experiment are neglected. However, these cooldown periods for different orbiter orientations (e.g., Sun facing and Earth viewing) could be incorporated in subsequent simulations of the flight experiment.

TABLE V.—TES EXPERIMENT SIMULATIONS

Simulation run	Lid mass, kg	PCM, K_{liq} , W/m-K
1	20.34	1.73
2	9.09	1.73
3	34.09	1.73
4	20.34	3.46

The first simulation in table V (run 1), is defined as the base case. The TES-1 experiment is placed in a conventional GAS can with no modifications. Estimates of power, peak temperatures, and freezing/melting times were established from run 1. Runs 2 and 3 differ from run 1 only in the GAS lid mass. Results from runs 1, 2, and 3 were used to determine the impact of the GAS lid mass on melting and solidification times. The fourth simulation (run 4) uses a LiF liquid thermal conductivity that is twice the value of the base case (run 1). According to reference 8, combined radiation and conduction through the liquid LiF can be approximated by using a thermal conductivity twice the value of K_{liq} . Run 4 was conducted to investigate the TES-1 experiment performance with the use of a more realistic approximation of the heat transfer through the PCM than the conservative approximation used for run 1. The solid phase of LiF is also translucent; however, this was not included in the run 4.

Both the initial heatup and the melt/freeze cycle scenarios remain the same for all four simulations. During the initial heat-up, the radiation shutter above the TES radiation flare remains closed. The heater is energized with a constant power of 260 W. The environmental temperature which is seen by the external surfaces of the GAS and the radiation shutter is 250 K. Typical environmental (sink) temperatures for an Earth view orbit are on the order of 250, while sink temperatures to deep space are generally less than 100 K. Results of initial heat-up simulation (heat-up time, heat-up energy, and TES specimen temperatures) are insensitive for environmental temperatures less than 300 K. Results of primary interest from the initial heatup scenario are the time to begin melting, the time of complete melting,

peak TES canister wall temperatures, heater power, and required heater energy.

The final temperatures from the initial heatup scenario were used as initial temperatures for the melt/freezing cycle simulation. Four and one half cycles, beginning with the solidification of the LiF and ending with the solidification of the LiF, were simulated. After complete solidification of the lithium fluoride, the melting portion of a given cycle was initiated. The melting process was completed after complete melting of the LiF. Details of the combined heating and cooling cycle simulation were presented earlier. The environmental, or sink, temperature during the melt/freezing simulation was 250 K. The external surface of the GAS lid and all external sides of the GAS can radiate to space (environment). The TES radiator flare radiates to the GAS lid during the PCM solidification. Simulation results are again not affected by sink temperatures of 300 K or less. All heat losses from the GAS are assumed to be by radiation to the environmental (sink) temperature.

Results and Discussion

Results consist of tabulated results provided in tables VI to IX, transient temperature profiles in appendix B, and color temperature contour plots in appendix C. The following nomenclature and definitions describe the results presented in tables VI to IX:

Compl Time	completion time from beginning of scenario
Delta Time	melting/freezing time per cycle
Heater Q	heater energy for given cycle

MLI Q	MLI heat loss during heating
MLI Pavg	average heat-loss power through MLI during heating portion of given cycle (MLI Q/Delta Time/60)
Base Q	heat loss from TES mounting base to node 109
Base Pavg	average heat-loss power through mounting base for corresponding Delta Time
U TES	PCM internal energy change for corresponding Delta Time
U Dot	average cooling or heating rate of PCM for corresponding Delta Time
Q Lat	PCM latent heat change for corresponding Delta Time
Q Sense	TES specimen (nodes 1 to 58) sensible heat change for corresponding Delta Time
T Lid	temperature of the GAS lid (node 108) at corresponding time into simulation, Compl Time
T Htr	peak temperature of heater nodes at corresponding time into simulation, Compl Time
T Canister -OD	peak temperature of outer TES canister wall at corresponding time into simulation, Compl Time

TABLE VI.—RUN 1 PHASE CHANGE COMPLETION RESULTS

[Lid mass, 20.3 kg.]

	Initial heatup	Cycle 1		Cycle 2		Cycle 3		Cycle 4		Cycle 5
		Solidification	Melting	Solidification	Melting	Solidification	Melting	Solidification	Melting	Solidification
Compl time, sec	7993.0	2015.0	5864.0	7872.0	11774.0	13773.0	17674.0	19674.0	23573.0	25573.0
Delta time, min	133.0	33.6	64.2	33.5	65.0	33.3	65.0	33.3	65.0	33.3
Heater Q, kJ	2078.3	-----	1001.0	-----	1015.0	-----	1014.0	-----	1014.0	-----
MLI Q, kJ	-236.0	-----	-202.2	-----	-218.0	-----	-218.0	-----	-218.0	-----
MLI Pavg, W	-29.6	-----	-52.5	-----	-55.8	-----	-55.8	-----	-55.8	-----
Base Q, kJ	-133.0	-42.3	-67.1	-42.1	-67.4	-41.8	-67.3	-41.8	-67.3	-41.8
Base Pavg, W	-16.6	-21.0	-17.4	-21.0	-17.3	-20.9	-17.3	-20.9	-17.3	-20.9
U TES, J	1709.0	-736.0	731.4	-731.4	729.2	-728.6	729.0	-729.0	728.9	-729.0
U Dot, W	213.8	-365.0	190.0	-364.0	186.9	-364.5	186.9	-364.4	186.9	-364.4
Q Lat, kJ	321.5	-321.5	321.5	-321.5	321.5	-321.5	321.5	-321.5	321.5	-321.5
Q Sense, kJ	1388.0	-414.6	409.9	-409.9	407.7	-407.2	407.6	-407.3	407.4	-407.4
T Lid, K	281.0	295.0	285.0	298.0	286.2	299.0	287.0	299.0	288.0	300.0
T Htr, K	1276.0	1026.0	1274.0	1026.0	1274.0	1026.0	1274.0	1026.0	1274.0	1026.0
T Canister-OD K	1237.0	1065.0	1234.0	1065.0	1234.0	1065.0	1234.0	1065.0	1234.0	1065.0

TABLE VII.—RUN 2 PHASE CHANGE COMPLETION RESULTS

[Lid mass, 9.1 kg.]

	Initial heatup	Cycle 1		Cycle 2		Cycle 3		Cycle 4		Cycle 5
		Solidification	Melting	Solidification	Melting	Solidification	Melting	Solidification	Melting	Solidification
Compl time, sec	8045.0	2005.0	5818.0	7826.0	11727.0	13727.0	17627.0	19628.0	23528.0	25528.0
Delta time, min	134.0	33.4	63.6	33.5	65.0	33.3	65.0	33.4	65.0	33.3
Heater Q, kJ	2091.7	-----	991.4	-----	1014.3	-----	1014.0	-----	1014.0	-----
MLI Q, kJ	-252.0	-----	-194.2	-----	-217.7	-----	-217.7	-----	-217.8	-----
MLI Pavg, W	-31.4	-----	-50.9	-----	-55.8	-----	-55.8	-----	-55.9	-----
Base Q, kJ	-133.6	-42.1	-66.5	-42.1	-67.4	-41.8	-67.3	-41.8	-67.3	-41.8
Base Pavg, W	-16.6	-21.0	-17.4	-21.0	-17.3	-20.9	-17.3	-20.9	-17.3	-20.9
U TES, J	1705.6	-732.0	730.8	-731.0	729.1	-728.7	729.0	-728.9	728.9	-728.6
U Dot, W	212.0	-36.5	191.7	-36.4	186.9	-364.3	186.9	-364.3	186.9	-364.3
Q Lat, kJ	321.5	-321.5	321.5	-321.5	321.5	-321.5	321.5	-321.5	321.5	-321.5
Q Sense, kJ	1384.1	-410.6	409.3	-409.5	407.7	-407.2	407.5	-407.5	407.4	-407.1
T Lid, K	276.0	298.1	282.0	301.5	283.1	302.7	283.9	303.2	284.3	303.4
T Htr, K	1275.0	1026.0	1274.0	1026.0	1274.0	1026.0	1274.0	1026.0	1274.0	1026.0
T Canister-OD K	1236.0	1065.0	1234.0	1065.0	1234.0	1065.0	1234.0	1065.0	1234.0	1065.0

TABLE VIII.—RUN 3 PHASE CHANGE COMPLETION RESULTS

[Lid mass, 34.1 kg.]

	Initial heatup	Cycle 1		Cycle 2		Cycle 3		Cycle 4		Cycle 5
		Solidification	Melting	Solidification	Melting	Solidification	Melting	Solidification	Melting	Solidification
Compl time, sec	8043.0	2005.0	5906.0	7905.0	11806.0	13806.0	17707.0	19706.0	23606.0	25606.0
Delta time, min	134.0	33.4	65.0	33.3	65.0	33.3	65.0	33.3	65.0	33.3
Heater Q, kJ	2091.2	-----	1014.0	-----	1014.3	-----	1014.3	-----	1014.0	-----
MLI Q, kJ	-252.3	-----	-218.0	-----	-217.7	-----	-217.9	-----	-217.6	-----
MLI Pavg, W	-31.4	-----	-55.8	-----	-55.8	-----	-55.8	-----	-55.8	-----
Base Q, kJ	-133.5	-42.1	-67.5	-41.8	-67.4	-41.8	-67.3	-41.8	-67.3	-41.8
Base Pavg, W	-16.6	-21.0	-17.3	-21.0	-17.3	-21.0	-17.3	-20.9	-17.3	-20.9
U TES, J	1705.5	-7320.4	729.1	-728.8	729.1	-729.1	729.1	-728.7	729.1	-729.0
U Dot, W	212.0	-36.5	186.9	-364.6	186.9	-364.6	186.9	-364.5	186.9	-364.5
Q Lat, kJ	321.5	-321.5	321.5	-321.5	321.5	-321.5	321.5	-321.5	321.5	-321.5
Q Sense, kJ	1384.0	-410.6	407.6	-407.4	407.7	-407.6	407.6	-407.3	407.6	-407.5
T Lid, K	284.8	294.0	286.8	295.7	288.0	296.7	288.8	297.4	289.3	297.8
T Htr, K	1275.0	1026.0	1274.0	1026.0	1274.0	1026.0	1274.0	1026.0	1274.0	1026.0
T Canister-OD K	1236.0	1065.0	1234.0	1065.1	1234.0	1065.0	1234.0	1065.0	1234.0	1065.0

All results in column 1 of the tables represent the final values from the initial heat-up scenario. All subsequent columns contain results from the melt/freeze cycle scenarios.

A comprehensive set of transient temperature profiles from run 1 is given in appendix B. Run 1 temperature profiles are shown for all the LiF PCM nodes (figs. B1 to B7); the TES canister inner and outer wall nodes 64 to 73 (figs. B8 and B9); heater nodes 97, 99, 101, and 103 (fig. B10); radiator surface nodes 11, 12, 14, 16, and 18 (fig. B11); conductor-rod nodes 11, 54, 56, and 58 (fig. B12); lid and GAS wall nodes 105 to 108 (fig. B13); mounting-base nodes 110, 111, and 112 (fig. B14); and spacer nodes 109 and 9109 (fig. B15). Figures B16 and B17 provide a comparison of temperature

profiles for runs 1, 2, and 3 of LiF PCM node 46, and the GAS lid node 108, respectively.

Six temperature contour plots are given in appendix C. Temperature contours of the TES specimen after completion of the initial heatup scenario and after the melt/freeze cycles scenario are shown in figures C.1 and C.2, respectively. Temperature contours for the overall GAS configuration are similarly shown in figures C.3 and C.4. Figure C.5 shows eight temperature contours from run 1 during the cycle-3 freezing and thawing process. The contours represent (a) the approximate first quarter of the freeze cycle, (b) the approximate midpoint of the freeze cycle, (c) the approximate third quarter of the freeze cycle, (d) complete solidification, (e) the approximate first quarter of the melt cycle, (f) the

TABLE IX.—RUN 4 PHASE CHANGE COMPLETION RESULTS

[Thermal conductivity, $2 \times \text{Liquid } K_{\text{LiF}}$]

	Initial heatup	Cycle 1		Cycle 2		Cycle 3		Cycle 4		Cycle 5
		Solidification	Melting	Solidification	Melting	Solidification	Melting	Solidification	Melting	Solidification
Compl time, sec	7878.0	1922.0	5670.0	7597.0	11343.0	13269.0	17016.0	18943.0	22688.0	24615.0
Delta time, min	131.3	32.0	62.5	32.1	62.4	32.1	62.5	132.1	62.4	32.1
Heater Q, kJ	2048.3	-----	974.5	-----	974.0	-----	974.0	-----	973.7	-----
MLI Q, kJ	-236.5	-----	-202.8	-----	-202.6	-----	-202.9	-----	-202.5	-----
MLI Pavg, W	-30.0	-----	-54.1	-----	-54.1	-----	-54.2	-----	-54.1	-----
Base Q, kJ	-131.6	-40.5	-65.9	-40.5	-65.7	-40.4	-65.7	-40.4	-65.6	-40.4
Base Pavg, W	-16.7	-21.1	-17.6	-21.0	-17.5	-21.0	-17.5	-21.0	-17.5	-21.0
U TES, J	1680.3	-705.7	705.8	-705.8	705.7	-705.4	705.6	-705.6	705.5	-705.5
U Dot, W	21.2	-367.0	188.3	-366.3	188.4	-366.2	188.3	-366.2	188.4	-366.1
Q Lat, kJ	213.3	-321.5	321.5	-321.5	321.5	-321.5	321.5	-321.5	321.5	-321.5
Q Sense, kJ	1358.8	-384.3	384.3	-384.3	384.2	-383.9	384.2	-384.1	384.1	-384.1
T Lid, K	281.0	294.4	284.5	297.1	286.2	298.4	287.2	299.2	287.7	299.6
T Htr, K	1258.0	1027.0	1258.0	1027.0	1258.0	1027.0	1258.0	1027.0	1258.0	1027.0
T Canister-OD K	1215.0	1066.0	1214.0	1066.0	1214.0	1066.0	1214.3	1066.0	1214.0	1066.0

approximate midpoint of the melt cycle, (g) the approximate third quarter of the melt cycle, and (h) complete melt. A temperature contour of the initial heatup scenario from run 4 is given in figure C.6 for comparison with the base case in figure C.1.

Base-case values of melting time, peak temperatures, and PCM heat changes for the initial heatup scenario are given in column 1 of table VI. During the initial heatup simulation, melting begins after approximately 1.5 hr. Complete melting occurs after 2.17 hr from the beginning of the initial heatup time. The peak canister wall temperature of 1237 K is less than the 1300 K limit imposed during the conceptual design of the TES experiment. This temperature is also the maximum temperature that occurs over both scenarios, the initial heatup and melt/freeze cycles. The TES specimen temperature contours in figure C3 indicate that the dominant direction of heat transfer is the radial direction. However, the heat losses from both the radiator flare and the mounting base which are evident in figure C3 also result in axial heat flow. Inspection of run 2 and run 3 initial heatup results in tables VII and VIII show negligible differences from the run 1 results.

The base-case heat loss from the TES specimen by radiation through the MLI and by conduction through the base is 366 kJ (the sum of rows 4 and 6 in table VI) for the initial heatup scenario. The radiative losses from the TES specimen are the heat losses from the MLI surrounding the TES specimen and the losses through the closed radiation shutter above the TES specimen. The average rate of heat loss (power) from the TES specimen through complete melting is 46 W. During the initial heatup of the TES specimen, the GAS temperatures decrease as shown in figure B13. The GAS wall temperatures are approximately 280 K at the completion of the initial heatup scenario. The tempera-

ture contour plot, figure C3, shows uniform GAS wall temperatures at the completion of the initial heatup while, temperature gradients exist throughout the TES specimen and mounting assembly.

Nominal cycle values of melting/freezing cycle times, temperatures, and PCM heat changes are given in table X. These values are obtained from the run 1 cycle results; however, they are also typical of runs 2 and 3. Melt and freeze times of 65 and 33 min are within acceptable limits of 1 hr +15 min -6 min and 34 min +6 min -4 min as specified in the TES Experiment Technical Requirements Document (TRD) (A NASA Lewis Internal Document prepared by David Namkoong in 1990).

TABLE X.—PREDICTED NOMINAL TES PERFORMANCE RESULTS PER THE MELT/FREEZE CYCLE

Melting time, min	65
Freezing time, min	34
Peak canister temperature, K	1234
Peak heater temperature, K	1274
Heater energy, kJ	1014
PCM latent heat change, kJ	322
TES specimen sensible heat change, kJ	407

During the melt/freeze cycles, the base-case canister-wall peak temperature is 1234 K, which is less than the peak temperature at the completion of the initial heatup scenario. Transient temperature profiles of LiF nodes are given in appendix B, figures B1 and B2. Specific node locations can be found from the node diagrams (figs. 5 and 7). The LiF PCM transient profiles in figures B1 to B5 show maximum subcooling of the PCM of approximately 90 K below the melting temperature of 1121.3 K. During heating, a temperature rise of approximately 85 K above melt temperature is observed for the PCM. The temperature contour plot

for the completion of cycle-5 solidification shows coolest temperatures at the radiator flare surface as expected. In addition, the temperature profile of the TES specimen is observed to be strongly two-dimensional. Mounting-base temperature gradients seen in the overall GAS configuration contours (figs. C3 and C4) result in the base conduction losses shown in tables VI to IX.

The base-case temperature contour plots in figure C5, show the freeze/melt process through the complete cycle 3. As solidification occurs, the LiF is observed to freeze inward from all TES canister walls. The lower central canister region is the last to freeze. It may be desirable to require LiF nearest the outer wall to freeze last, as suggested in the 1990 NASA Lewis Internal TES Technical Requirements Document by David Nankoong. Therefore, applying a small amount of power to the heater may be necessary during the solidification process. During the early stages of melting, as shown in figures C5(e) and (f), heat flow in the PCM is primarily in the radial direction. At the completion of melting (fig. C5(h)) the lower portions of the conductor rod and PCM are observed to have cooler temperatures. These cooler temperatures result from the conduction losses to the mounting base.

The TES specimen heat losses through the MLI and through the base during the heating portion of a cycle were 218 and 67 kJ, respectively. The resulting average heat loss rates were 56 and 17 W for the MLI and base, respectively. Recall that an estimated or desired value of the average MLI heat loss rate is used to determine the MLI effectiveness as discussed in the Model Geometry and Thermal Properties section. Summing the TES internal energy change and heat losses (rows 4, 6, and 8 in table VI) during the heating portion of the third cycle yields 1003 kJ. The resulting variation with the heater energy input is small (1.1 percent).

A comparison of tables VI to VIII reveals that the only noticeable difference among runs 1, 2, and 3 is the lid temperature during the melt/freezing scenario. The PCM temperature profiles for LiF node 46 are plotted in figure B16 for runs 1, 2, and 3. The maximum and minimum temperatures of the three runs are the same. However, the melt/freezing cycle times of the smallest mass GAS lid (run 2) lag the simulations with larger GAS lid masses. The lagging of the run-2 temperature profile increases in each cycle. Figure B17 shows a comparison of transient temperature profiles for the GAS lid, node 108, from runs 1, 2, and 3. Run 2, which has the smallest GAS lid mass (9.1 kg), shows the largest temperature swings and the greatest temperature rise with each cycle. The increasing lag of the run-2 temperature profile in figure B16 may be caused by the gradual increase in GAS lid temperature in subsequent cycles. An increase in lid temperature also causes an increase in freezing time. Run 3, which has the largest

TABLE XI.—GAS LID TEMPERATURE RISE
AS FUNCTION OF LID MASS

Simulation run	Lid mass, kg (lb)	Lid temperature rise, K
1	20.34 (44.25)	19.0
2	9.091 (20)	27.4
3	34.09 (75)	13.0

GAS lid mass (34.1 kg), shows the smallest temperature swing and smallest temperature rise per cycle. Table XI gives the temperature rise of the GAS lid during the 4.5 freeze/melt cycles for different GAS lid masses (simulations).

Run 4 represents a more realistic simulation of the TES experiment by attempting to account for heat transferred to the LiF by radiation in addition to the heat transferred by conduction. An approximation to account for the radiative contribution is suggested in reference 8. This approximation consists of simply doubling the liquid thermal conductivity value of the LiF. Comparison of the run-4 simulation results with those of the base case, run 1, reveals that the melting and freezing times will decrease by approximately 2.5 and 1.2 min, respectively. The canister-wall peak temperature of 1215 is 22 K lower than that of the base case. These comparisons translate into a 3.2-percent decrease in the TES specimen internal energy change and a 4-percent decrease in heater energy per cycle with respect to the base case. Figure C6 shows the cooler temperatures of the heater, canister walls, conductor rod, and radiator flare at the completion of the initial heatup from run 4.

Concluding Remarks

An approach for modeling phase change using thermal analyzers was successfully developed and implemented. The advantages of this approach with respect to the effective Cp approach are insensitivity to computer roundoff error and ability to maintain a constant phase change temperature. The method is applicable to thermal analyzers that solve the energy equation in terms of temperature (this includes most commercial analyzers). The method can be incorporated into thermal analyzers, such as SINDA, which permit access to basic solution variables (i.e., temperatures, thermal capacitances, and thermal conductances).

The thermal model was developed to provide conservative estimates of required heater energy, melting and freezing times, and peak temperatures. Conservative, for this analysis, implies greater predicted heater energy, larger predicted times and hotter predicted peak temperatures with respect to actual values. For all simulations, the cycles were repeatable after the first melt/

freeze cycle, and the PCM freezing and melting times were within acceptable limits. Peak temperatures of the PCM canister did not exceed the 1300 K temperature limit. The aluminum GAS wall temperatures never exceeded 300 K, which is well below GAS or electronic components overheat (failure) temperature limits. Three simulations were performed to investigate the effects of the GAS lid mass on the melting and freezing times of the PCM. Results from the lid mass comparison indicate negligible effect on the freezing and melting times for GAS lid masses from 9.1 to 34.1 kg. Therefore, the use of a lid mass between 9.1 and 34.1 kg will not affect the TES experimental results. The fourth simulation uses a simple approximation to account for combined radiation and conduction transport through the liquid LiF (the semitransparent nature of the solid phase was not included). Comparison of the simulation results with those of the base case, run 1, reveals that the melting and freezing times will decrease by approximately 2.5 and 1.2 min, respectively, while the peak canister wall temperature is 22 K lower than the base case. The liquid semitransparent approximation results in 3.9-, 3.8-, and 2-percent decreases in freezing times, melting times, and peak canister temperatures with respect to conduction only. The TES specimen internal energy change and heater energy per cycle decrease by 3.2 and 4 percent, respectively, compared to the base case. For all simulations, the influence of buoyance or surface tension driven convection is expected to reduce melting/freezing times and peak PCM canister temperatures.

The thermal model and results can be used to evaluate (benchmark) new computer programs or models that

have been developed to predict solid/liquid phase change behavior. Specifically, results are provided for benchmarking combined conduction and phase change capabilities of the unverified computer programs or models.

Acknowledgments

This work was initiated at the request of Bob Migra and Ted Mroz who originally conceived of the TES Flight Experiment and TES Program. Further modifications to the model were performed in support NASA Lewis' Space Flight Branch which assumed responsibility of the TES flight experiment. Model results generated herein and report preparation were funded by the Solar Dynamic and Thermal Management Branch, under the direction of Jim Calogeras. Dave Namkoong, the TES program manager, helped to focus both the model development and the subsequent model summary. Eric Kelly provided technical guidance during the initial SINDA model development. Finally, Ted Mockler, former lead thermal analyst for the TES Flight Experiment, provided many valuable suggestions that were incorporated into the model. He also performed comprehensive reviews during various stages of the modeling.

Lewis Research Center
National Aeronautics and Space Administration
Cleveland, Ohio, August 14, 1991

Appendix A

Finite Difference Solutions and Development of Phase Change Initiation Logic

Three finite difference forms of the energy equation - explicit, implicit, and explicit/implicit (Crank-Nicholson approximation) - are given in equations (A1) to (A3). All three equations consist of the sensible heat storage term, a heat-source term, and conduction terms. For the present discussion, other possible terms such as radiation conductance terms are neglected.

$$\frac{C_i(T_{i,n+1} - T_{i,n})}{\Delta t} = Q_i + \sum_{j=1}^N [G_{ji}(T_{j,n} - T_{i,n})] \quad (\text{explicit}) \quad (\text{A1})$$

$$\frac{C_i(T_{i,n+1} - T_{i,n})}{\Delta t} = Q_i + \sum_{j=1}^N [G_{ji}(T_{j,n+1} - T_{i,n+1})] \quad (\text{implicit}) \quad (\text{A2})$$

$$\frac{C_i(T_{i,n+1} - T_{i,n})}{\Delta t} = Q_i + 0.5 \sum_{j=1}^N [G_{ji}(T_{j,n} - T_{i,n})] + 0.5 \sum_{j=1}^N [G_{ji}(T_{j,n+1} - T_{i,n+1})] \quad (\text{Crank-Nicholson}) \quad (\text{A3})$$

Rearranging equation (A1) to solve for $T_{i,n+1}$ leads to equation (A4).

$$T_{i,n+1} = T_{i,n} + \frac{\Delta t}{C_i} \left\{ Q_i + \sum_{j=1}^N [G_{ji}(T_{j,n} - T_{i,n})] \right\} \quad (\text{A4})$$

From equation (A4) we see that the temperature of an i th node at the new time value, t_{n+1} , can be "explicitly" solved for in terms of node temperatures at the old time, t_n . Therefore, any temperature at the new time,

t_{n+1} , can be computed immediately and independently. From inspection of equations (A2) and (A3), we note that $T_{i,n+1}$ is also dependent on the other node temperatures, T_j 's at time, t_{n+1} . The implicit and Crank-Nicholson solution schemes are attractive because they are unconditionally stable (not necessarily correct).

The CG_{\min} , $C_i/\sum G_{ji}$, is an indicator of the maximum stable time step size for an explicit solution for the TES thermal model the CG_{\min} varies approximately two orders of magnitude. Therefore, the Crank-Nicholson solution routine (SINDA/FLUINT Subroutine FWDBCK) was chosen for this analysis. The exact finite difference equation that is solved in subroutine FWDBCK is given in equation (A5).³

$$\begin{aligned} \frac{2C_i(T_{i,n+1} - T_{i,n})}{\Delta t} = & 2Q_i + \sum_{j=1}^N \left\{ G_{ji}(T_{j,n} - T_{i,n}) \right. \\ & + G_{ji}[T_j^4 - T_i^4] \left. \right\} \\ & + \sum_{j=1}^N \left\{ G_{ji}(T_{j,n+1} - T_{i,n+1}) \right. \\ & + G_{ji}[T_{j,n+1}^4 - T_{i,n+1}^4] \left. \right\} \quad (\text{A5}) \end{aligned}$$

The latent heat contribution, Q_i , in the $m\Delta t_{m+1}$ time step is exactly equal to $Q_{i,os}$ (computed from eq. (4)) for an explicit solution routine. The equivalence of Q_i and $Q_{i,os}$ for an explicit finite difference solution is demonstrated below.

First, we rewrite the explicit finite difference equation (A1) in a form given by equation (A6), which will allow us to apply the phase-change initiation scheme described in the section titled Simulation of Combined Heating and Cooling Cycles. The superscript k denotes the k th iteration at the $m\Delta t_{m+1}$ time step.

$$\frac{C_i({}^kT_{i,n+1} - T_{i,n})}{\Delta t} - {}^kQ_i = \sum_{j=1}^N G_{ij}(T_{j,n} - T_{i,n}) \quad (\text{A6})$$

The remaining term on the right side of equation (A6) is invariant with k . Therefore, we can equate the left side of equation (A6) for the 0th and 1st iterations as shown in equation (A7).

³Cullimore, B.A., et al.: SINDA '85/FLUINT User's Manual, Version 2.3. NASA Contract NAS9-17448; MCR-90-512, Martin Marietta Corporation, Denver, CO, 1990.

$$\frac{C_i(^{\circ}T_{i,n+1} - T_{i,n})}{\Delta t} - {}^{\circ}Q_i = \frac{C_i(^1T_{i,n+1} - T_{i,n})}{\Delta t} - {}^1Q_i \quad (A7)$$

The temperature ${}^{\circ}T_{i,n+1}$ by definition is also the overshoot temperature, $T_{i,os}$, while ${}^{\circ}Q_i = 0$. Substituting ${}^{\circ}T_{i,n+1}$ and ${}^{\circ}Q_i$ into equation (6) gives equation (A8) for 1Q_i .

$${}^1Q_i = \frac{C_i(T_{lat} - T_{i,os})}{\Delta t} \quad (A8)$$

Substituting equation (A8) into equation (A7) and simplifying yields equation (A9).

$$T_{i,os} - T_{i,n} = (^1T_{i,n+1} - T_{i,n}) - (T_{lat} - T_{i,os}) \quad (A9)$$

Both $T_{i,os}$ and $T_{i,n}$ cancel out of equation (A9) leaving the result:

$${}^1T_{i,n+1} = T_{lat}$$

Since ${}^1T_{i,n+1} = T_{lat}$, ${}^2Q_i = {}^1Q_i$, which satisfies the convergence criteria given by equation (7). In summary,

equation (4) immediately (no further iterations) gives the latent heat contribution in the ${}_m\Delta t_{m+1}$ time step for an explicit finite difference solution.

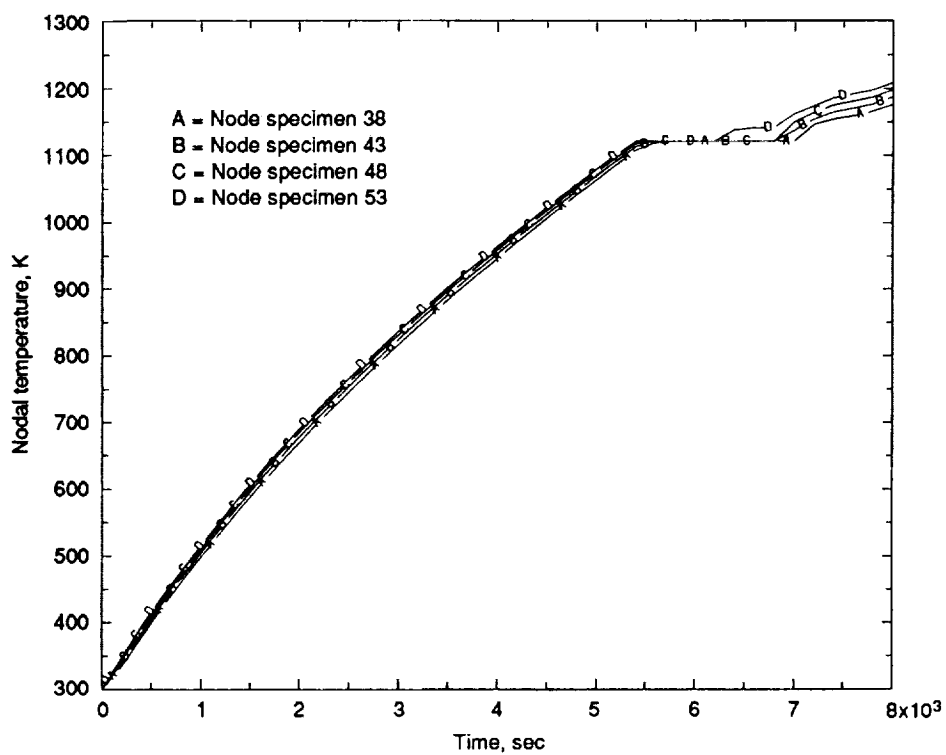
By applying a similar argument to an implicit finite difference solution, equation (A2), is rewritten as equation (A10). The temperatures on the right side of equation (A10) are computed at $t=t_{n+1}$. Therefore, superscript k is now required on these terms.

$$\frac{C_i(^kT_{i,n+1} - T_{i,n})}{\Delta t} - {}^kQ_i = \sum_{j=1}^N G_{i,j} (^kT_{j,n+1} - {}^kT_{i,n+1}) \quad (A10)$$

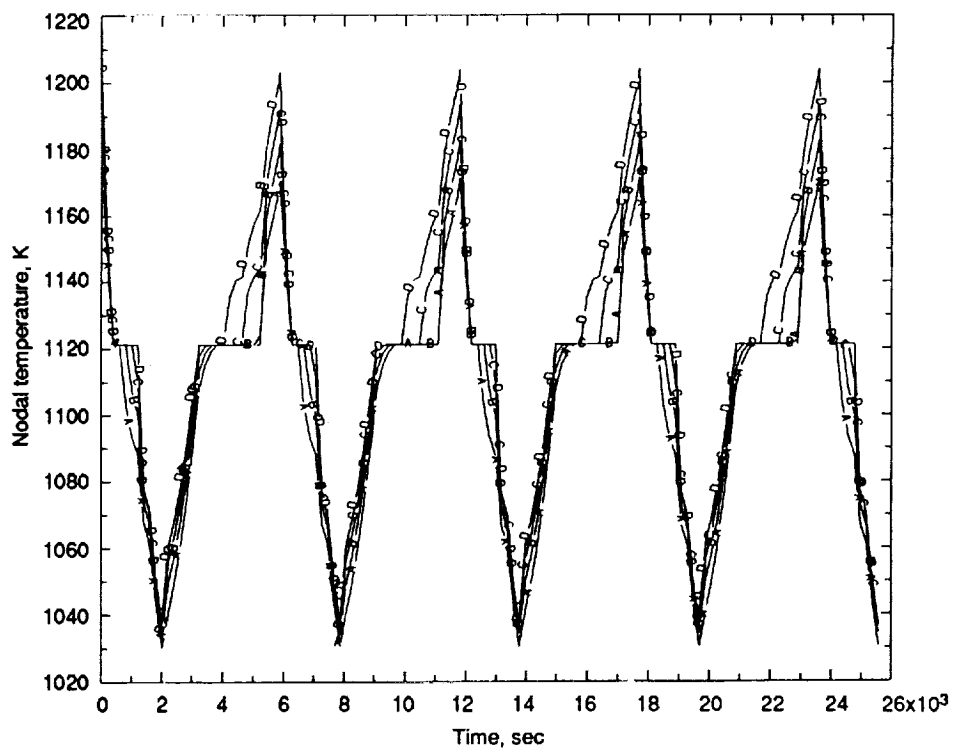
In contrast to equation (A6), the right side of equation (A10) not invariant with k . Since all temperatures at the time $= t_{n+1}$ must be solved for simultaneously, any change in $T_{i,n+1}$ affects all other temperatures, $T_{j,n+1}$'s. Hence, an iterative scheme such as the one developed in the section on Simulation of Combined Heating and Cooling Cycles is required to determine the latent heat contribution during the ${}_m\Delta t_{m+1}$ time step (initiation of phase change).

Appendix B

Transient Temperature Profiles for Selected TES Components and Nodes

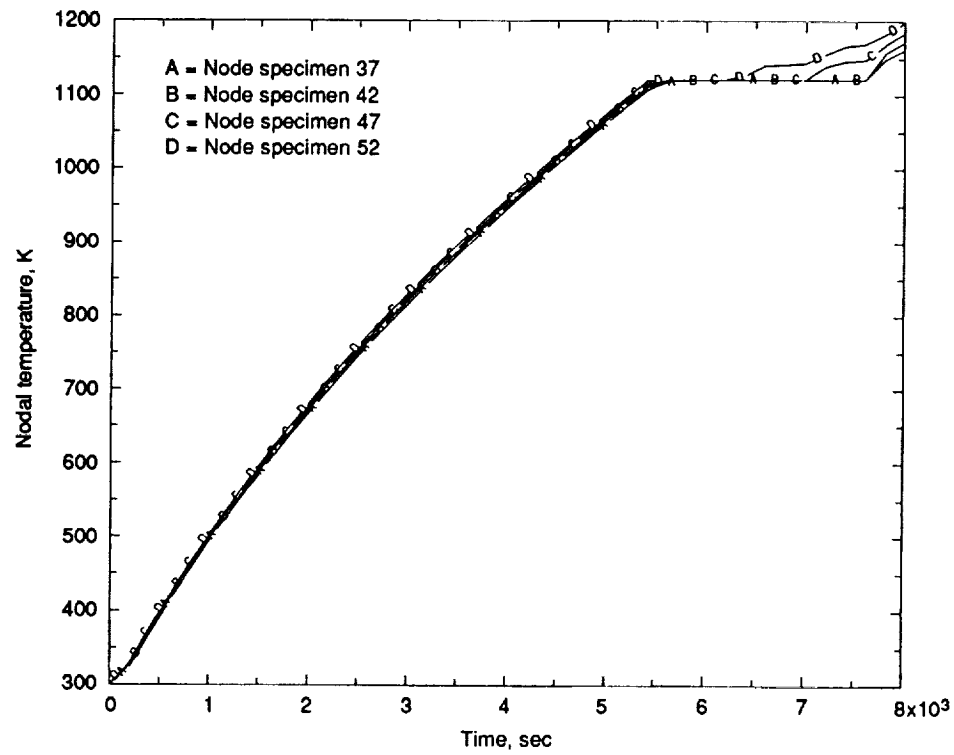


(a) Initial heatup scenario.

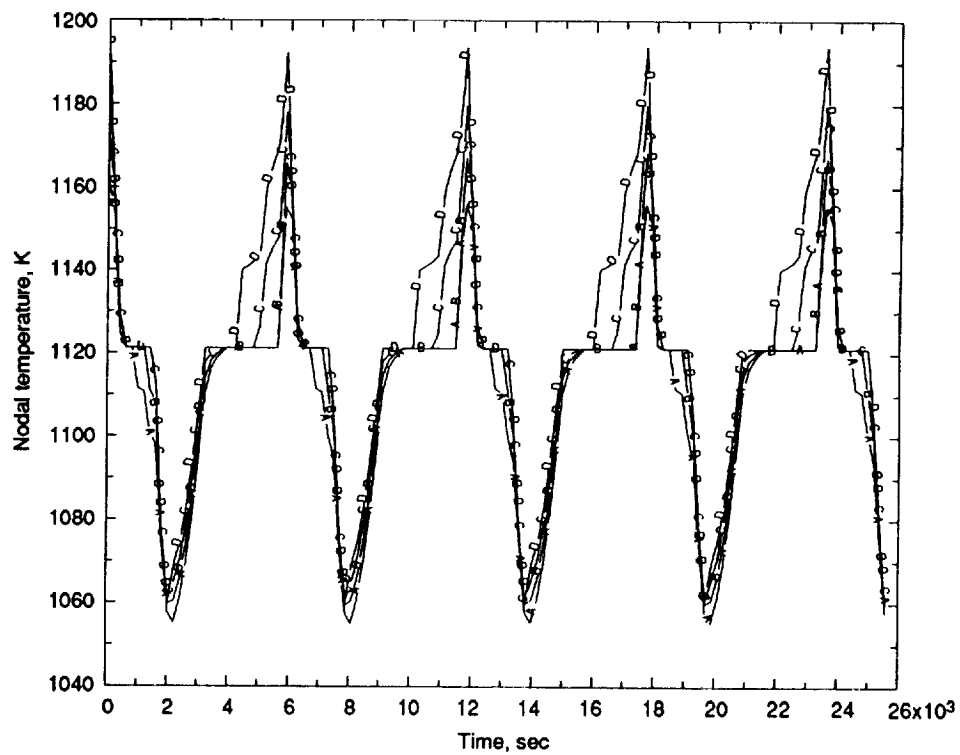


(b) Freeze/melt cycle scenario.

Figure B1.—LiF nodes, row 1.

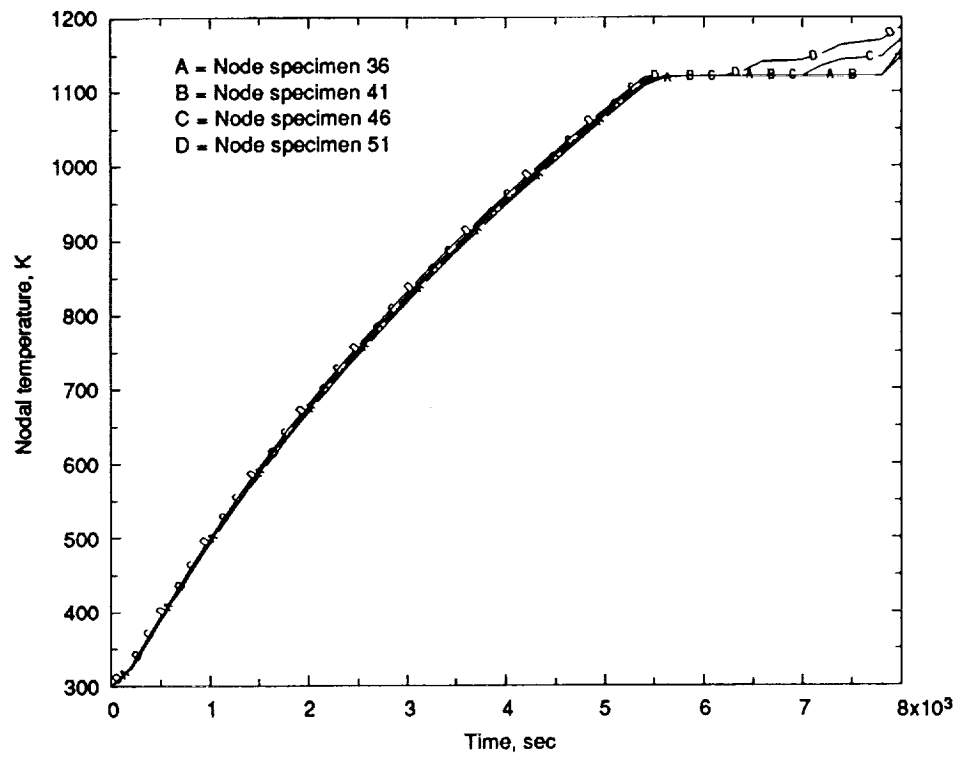


(a) Initial heatup scenario.

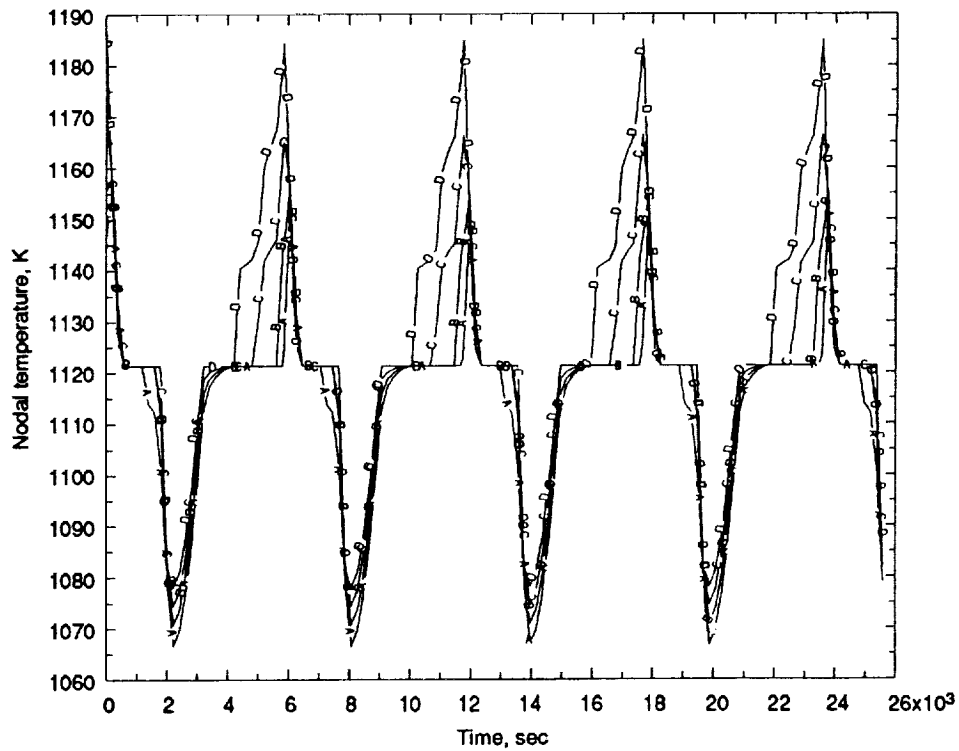


(b) Freeze/melt cycle scenario.

Figure B2.—LiF nodes, row 2.

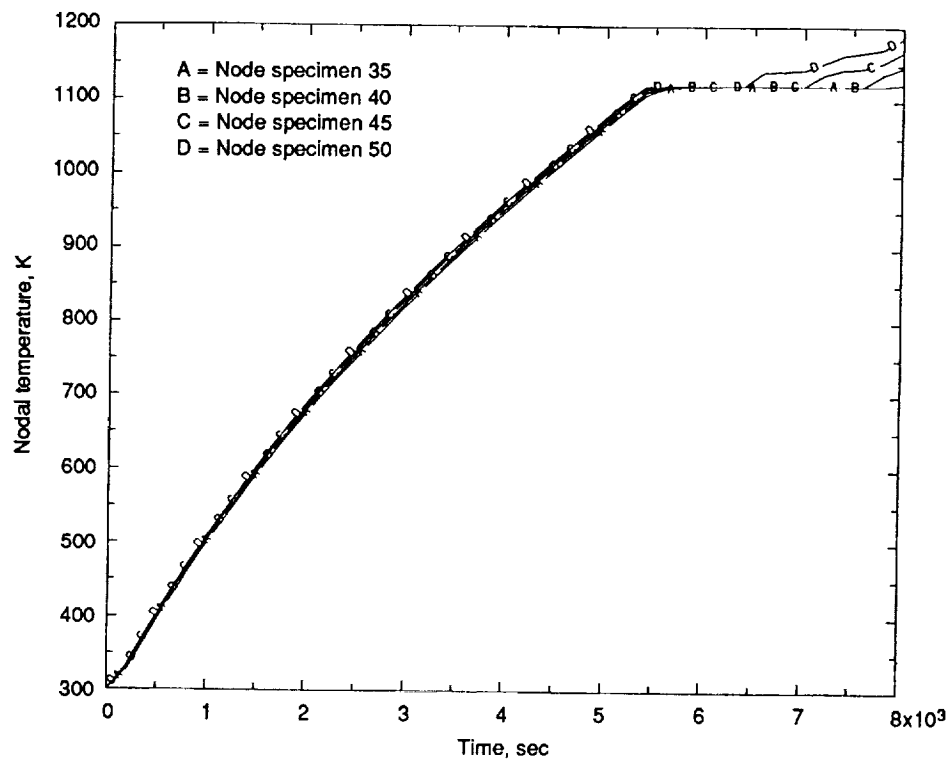


(a) Initial heatup scenario.

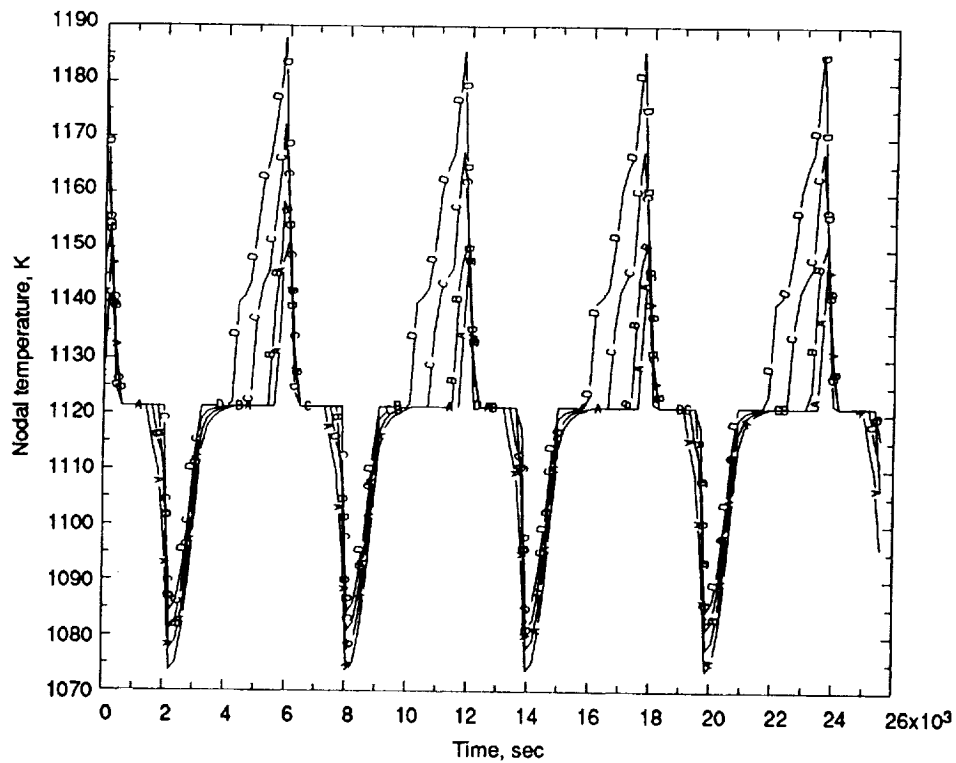


(b) Freeze/melt cycle scenario.

Figure B3.—LiF nodes, row 3.

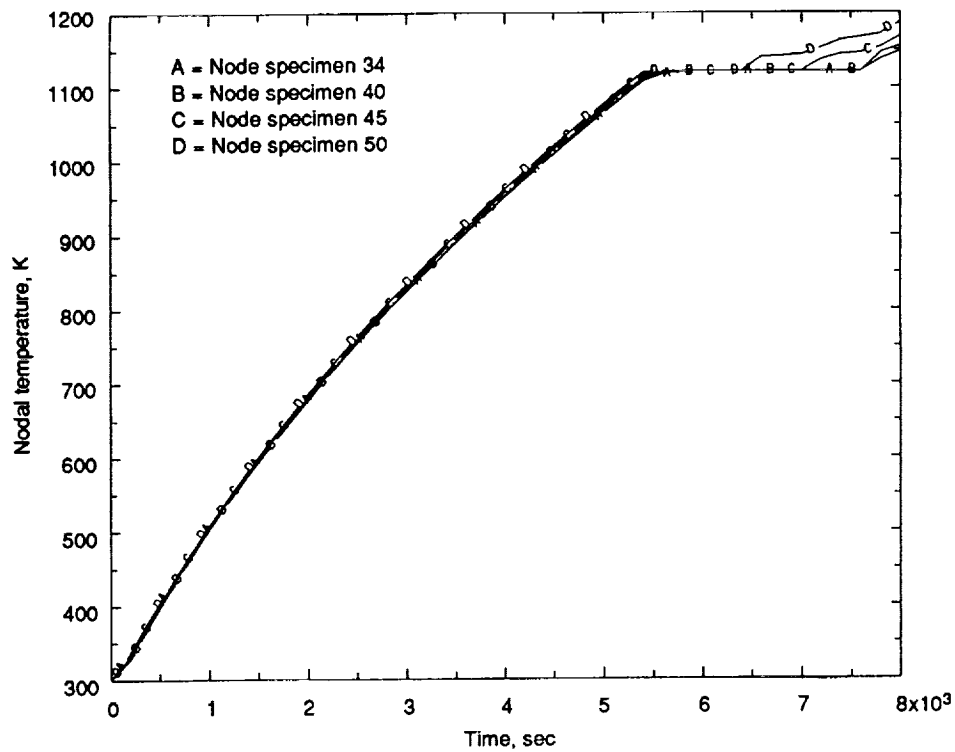


(a) Initial heatup scenario.

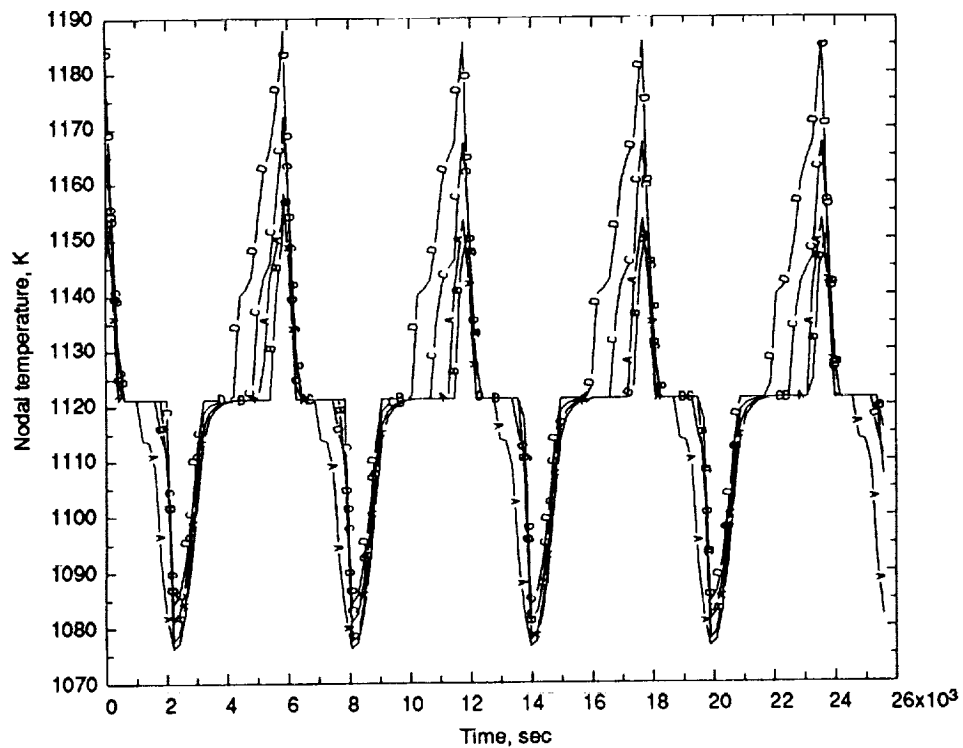


(b) Freeze/melt cycle scenario.

Figure B4.—LiF nodes, row 4.

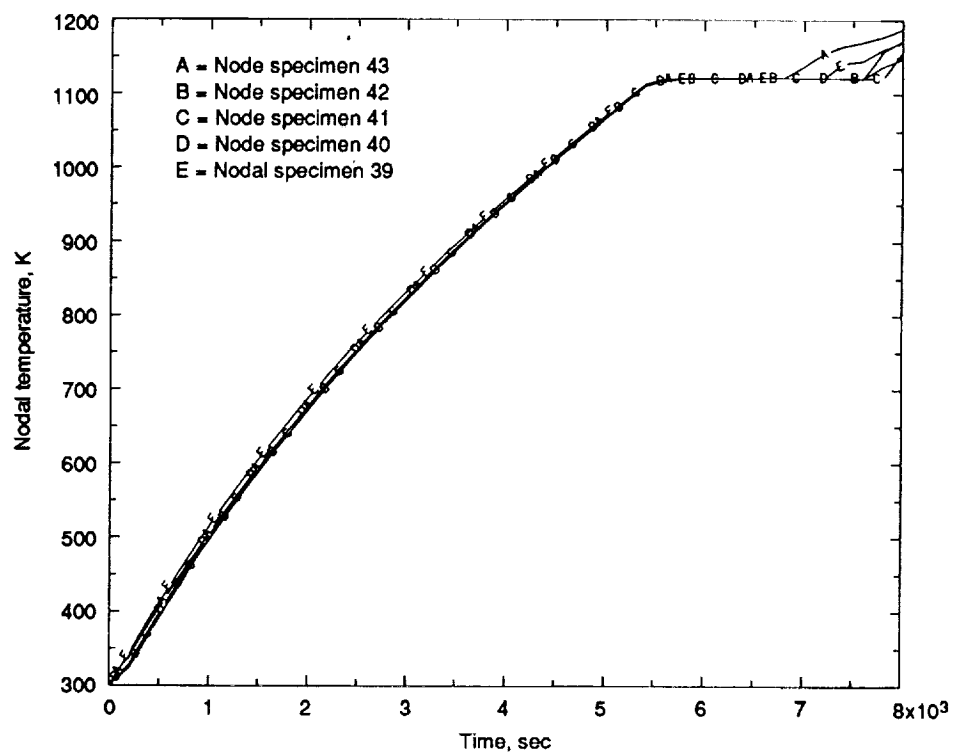


(a) Initial heatup scenario.

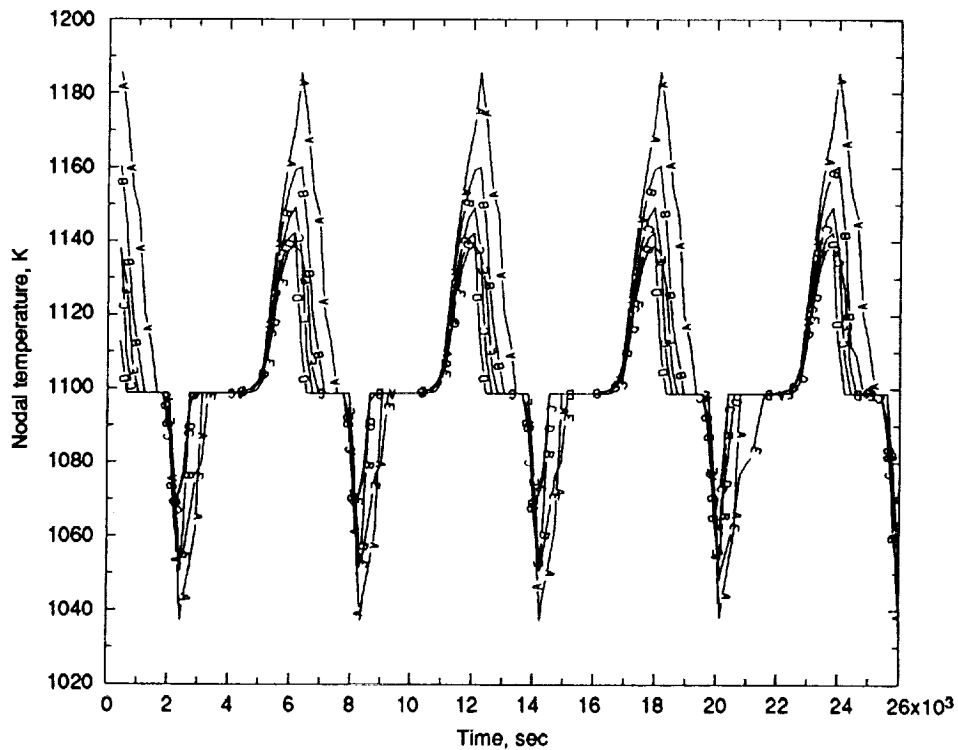


(b) Freeze/melt cycle scenario.

Figure B5.—LiF nodes, row 5.

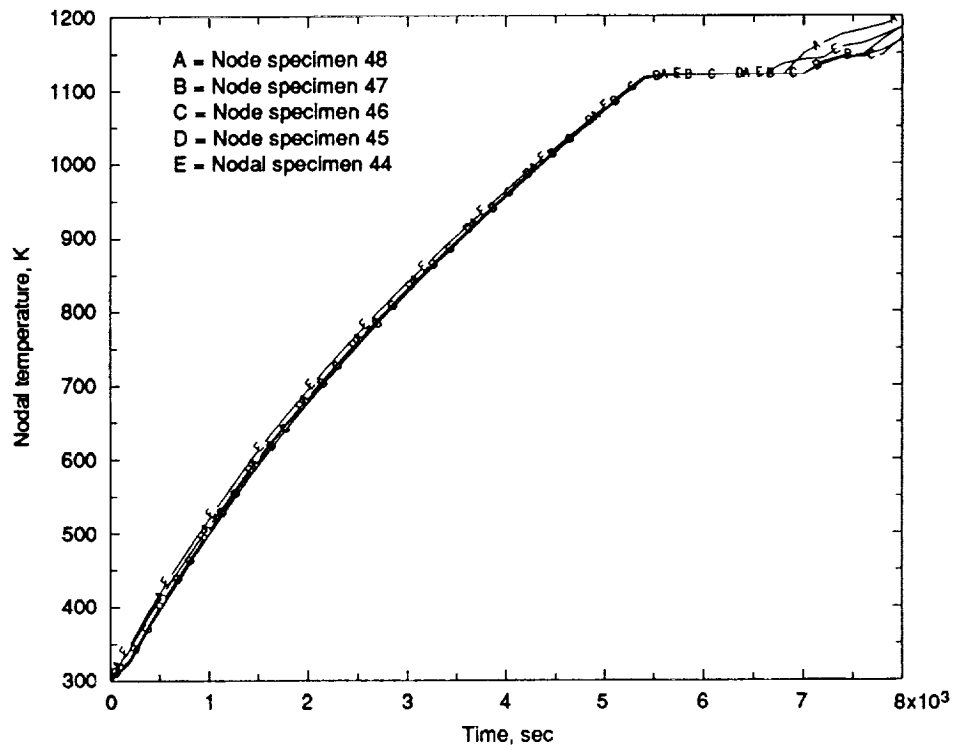


(a) Initial heatup scenario.

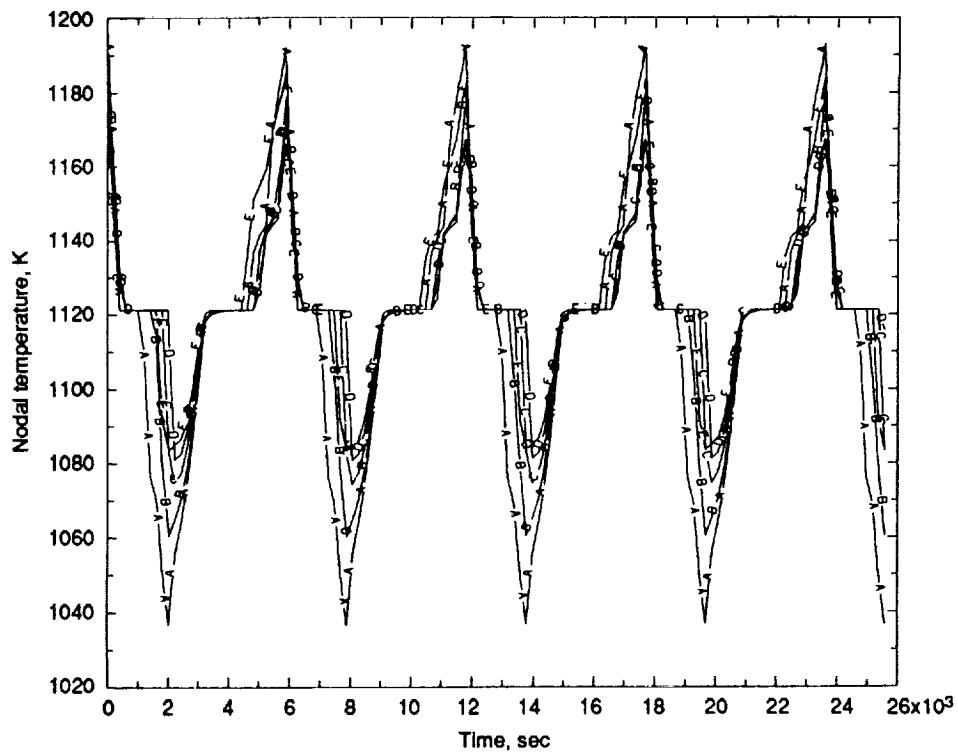


(b) Freeze/melt cycle scenario.

Figure B6.—LiF nodes, column 2.

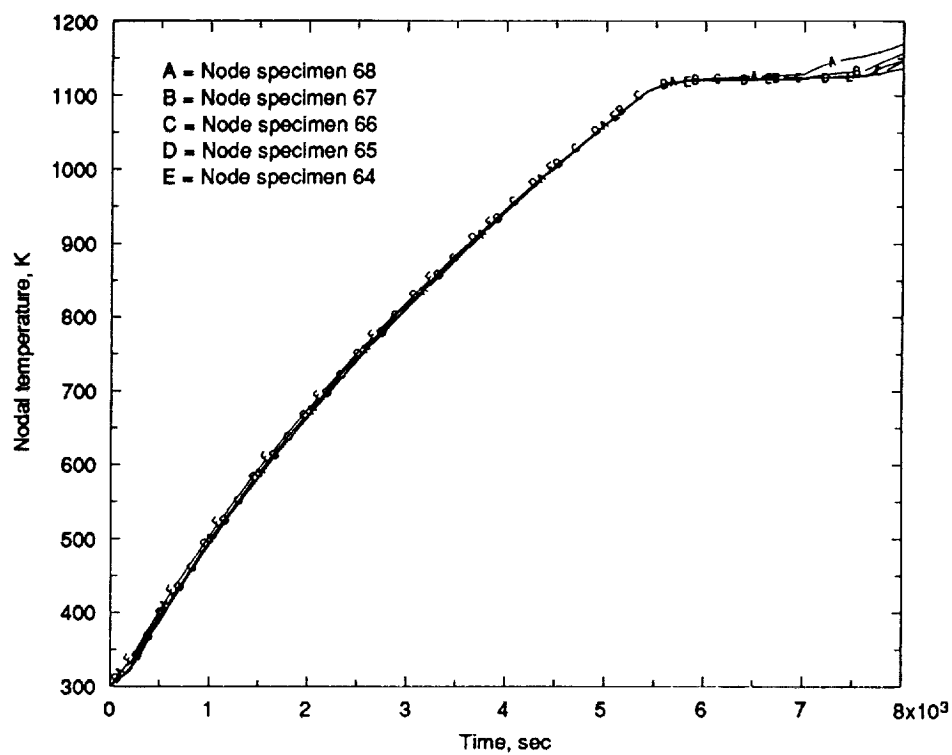


(a) Initial heatup scenario.

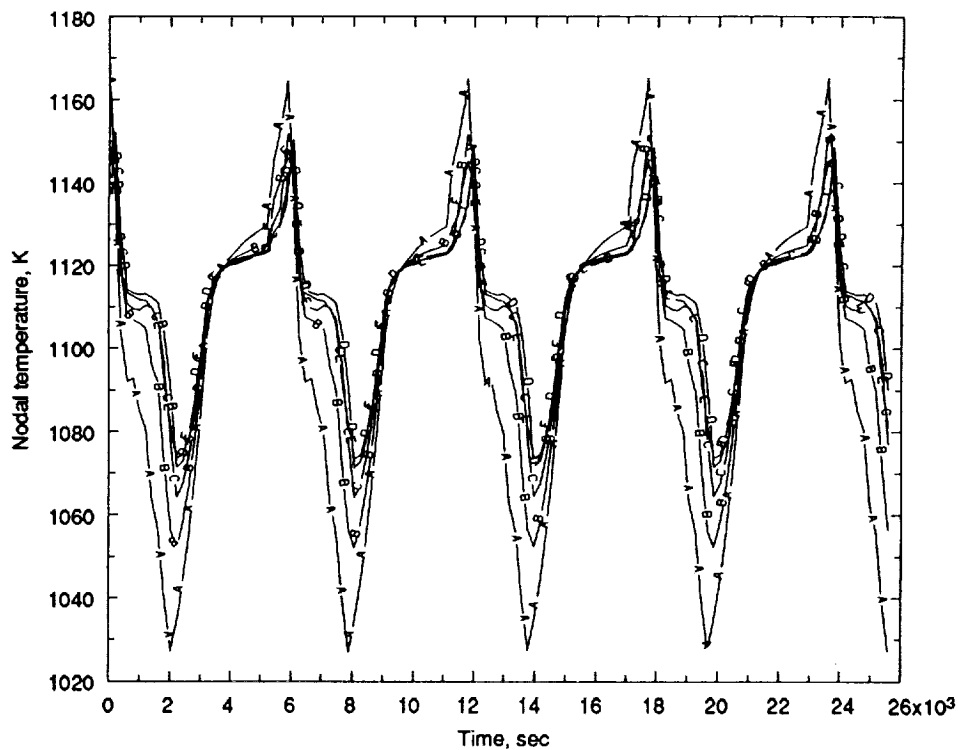


(b) Freeze/melt cycle scenario.

Figure B7.—LIF nodes, column 3.

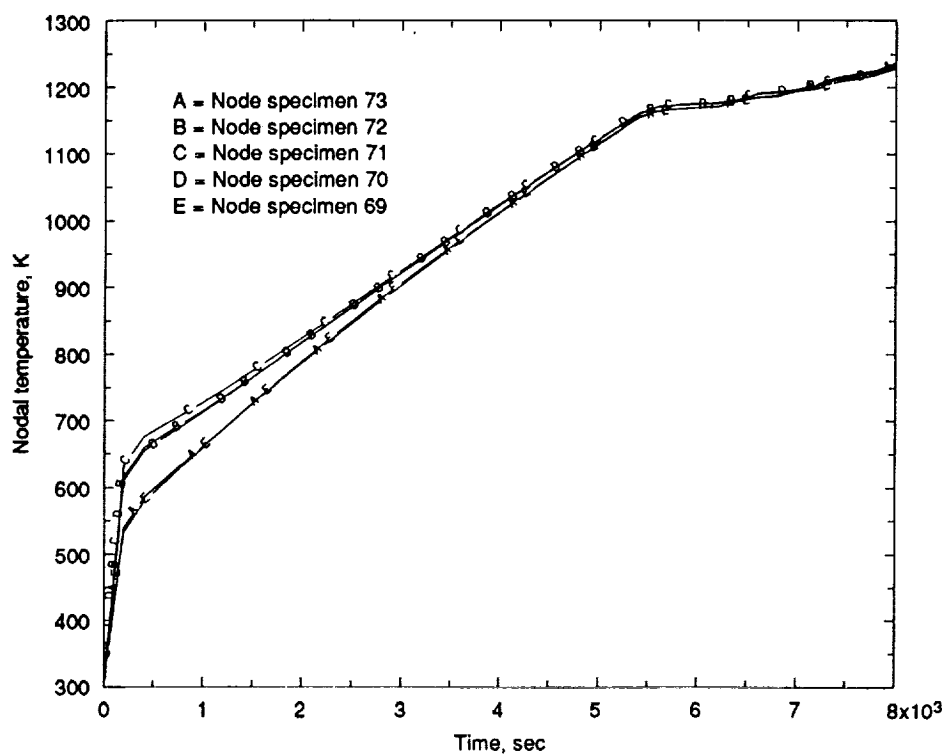


(a) Initial heatup scenario.

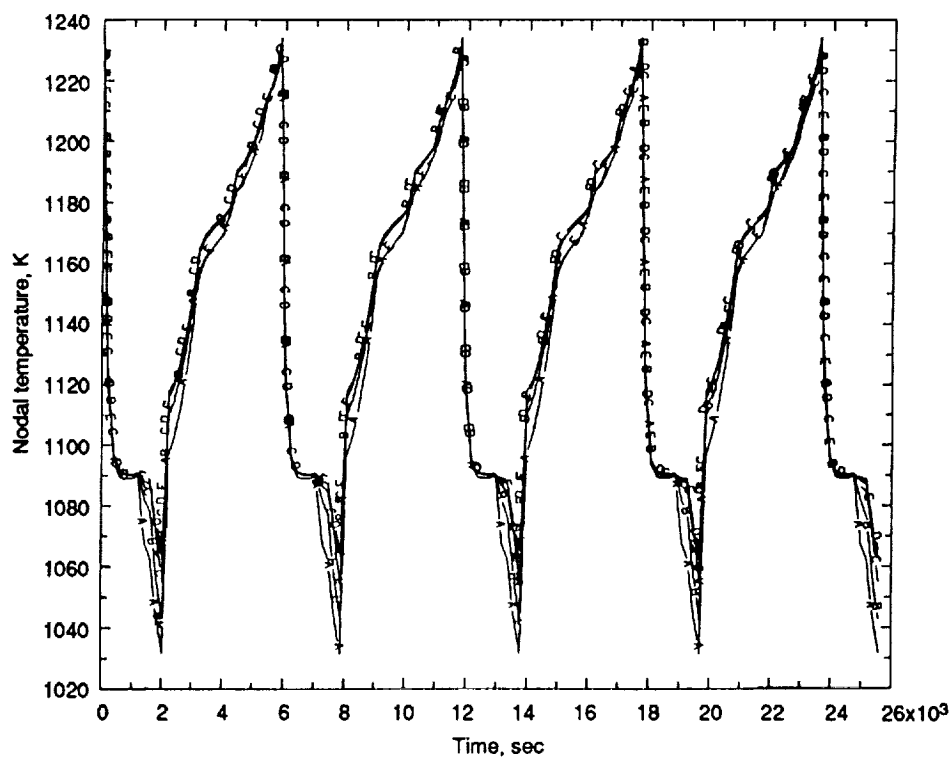


(b) Freeze/melt cycle scenario.

Figure B8.—Canister inner-wall nodes.

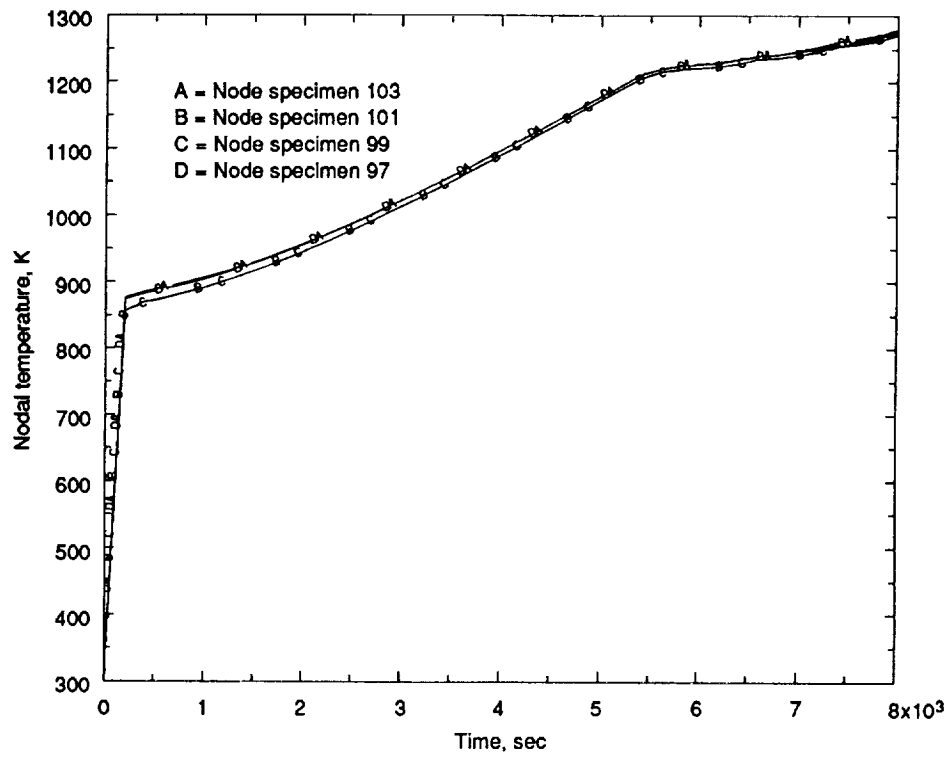


(a) Initial heatup scenario.

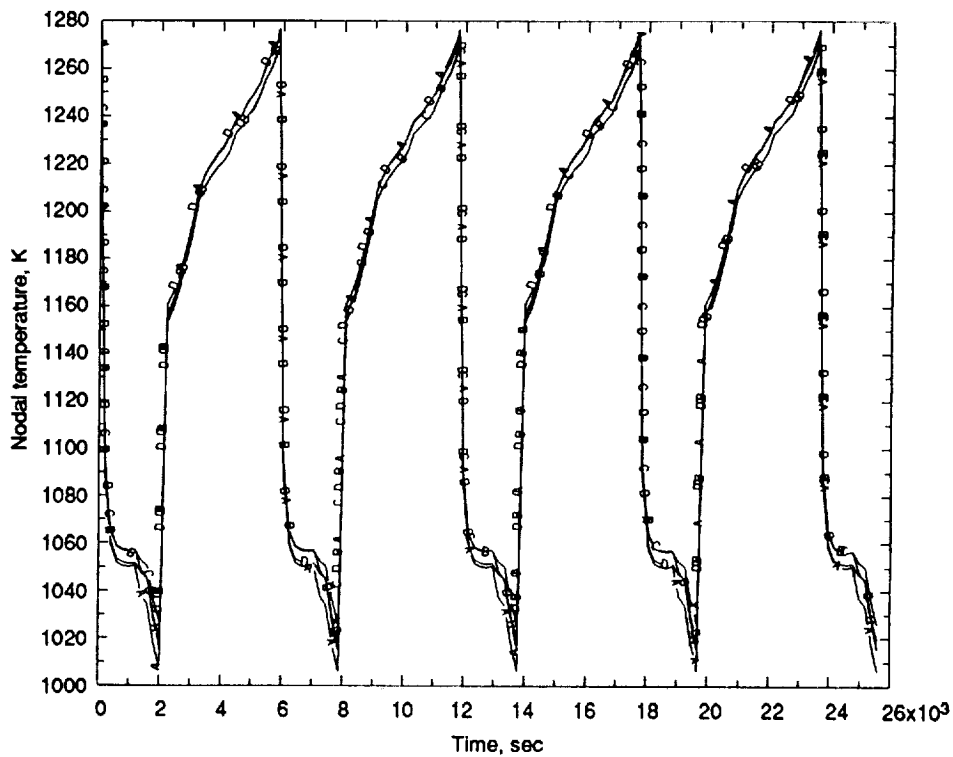


(b) Freeze/melt cycle scenario.

Figure B9.—Canister outer-wall nodes.

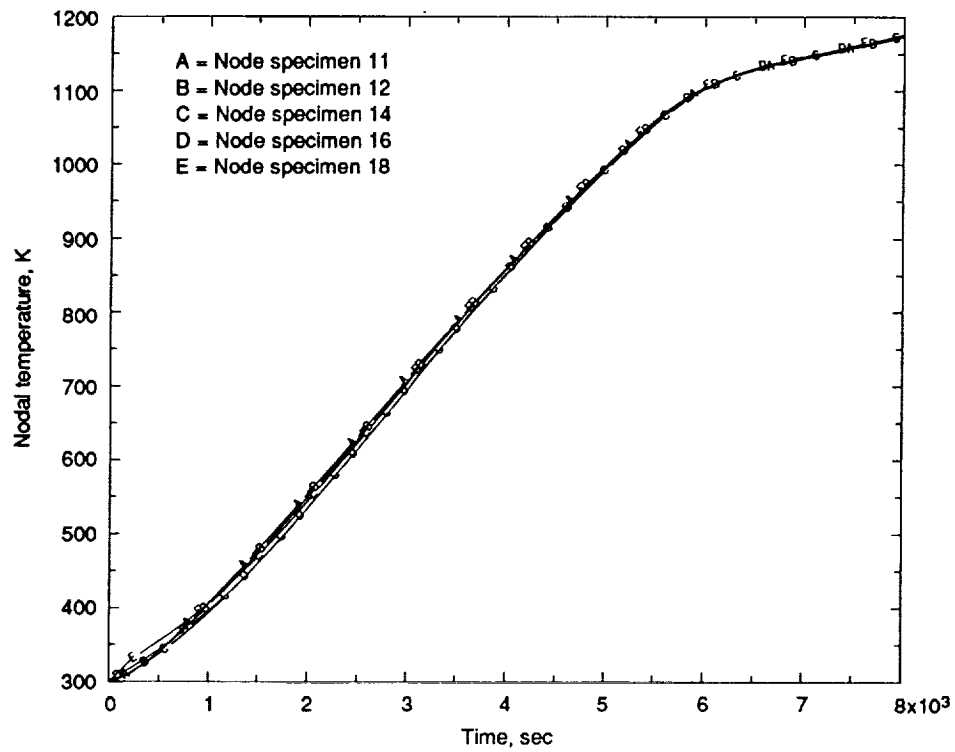


(a) Initial heatup scenario.

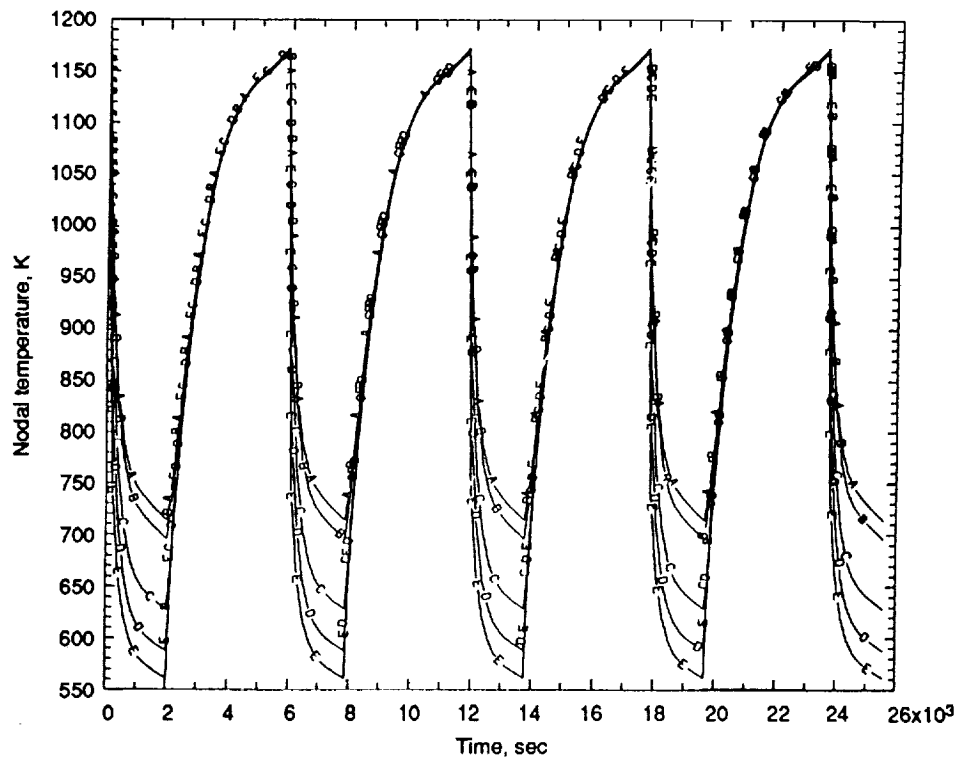


(b) Freeze/melt cycle scenario.

Figure B10.—Heater nodes.

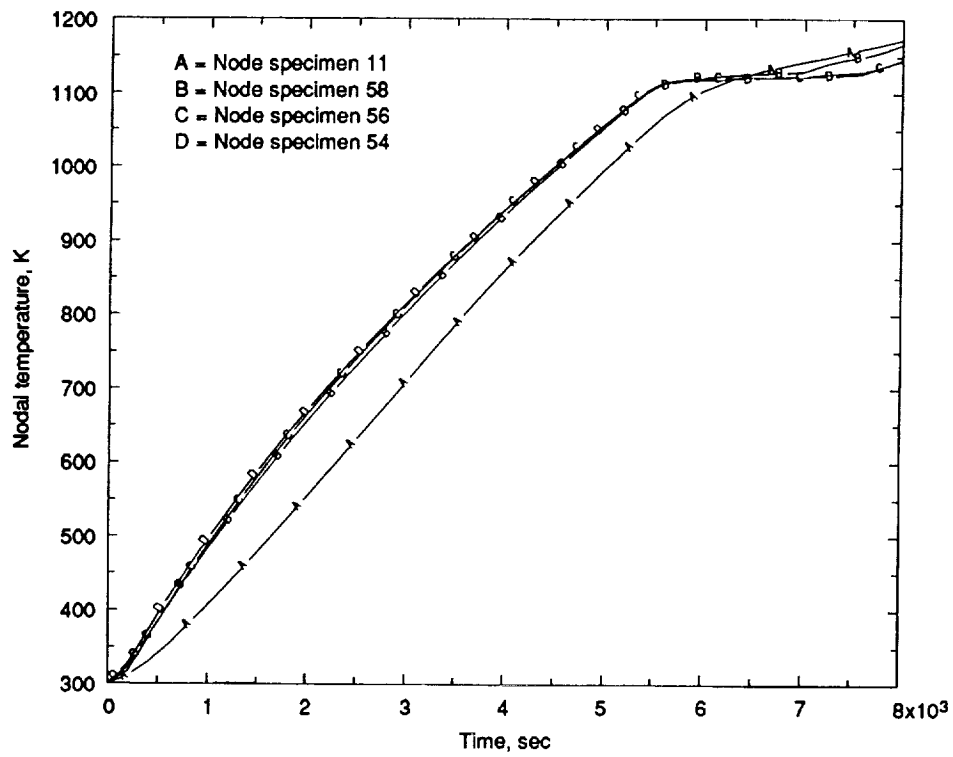


(a) Initial heatup scenario.

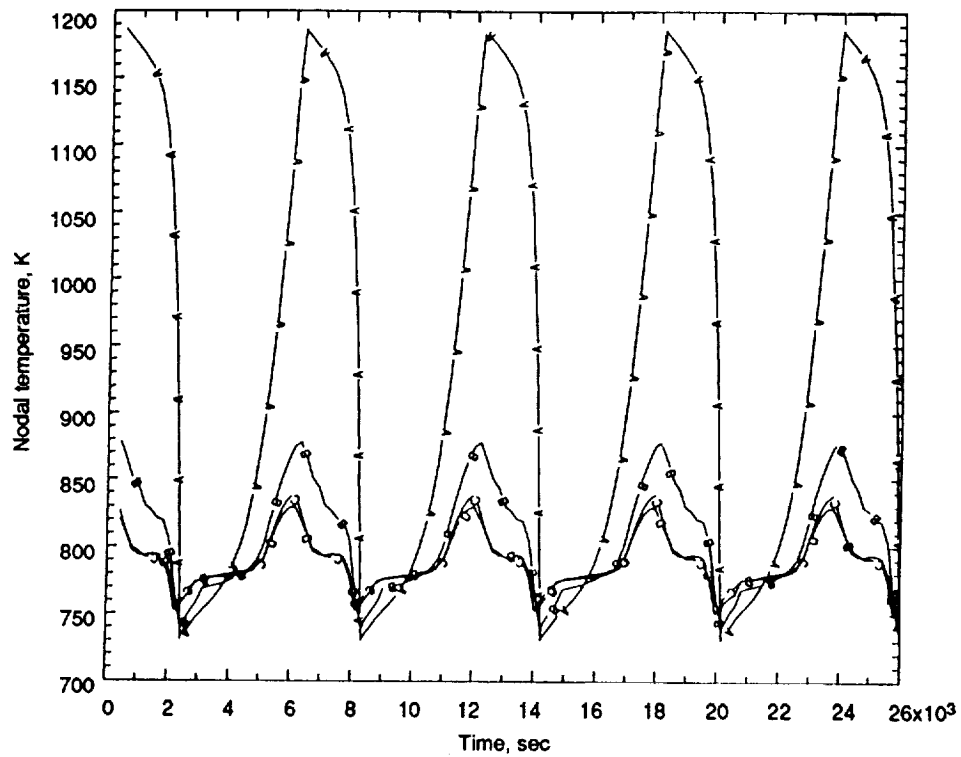


(b) Freeze/melt cycle scenario.

Figure B11.—Radiator surface nodes.

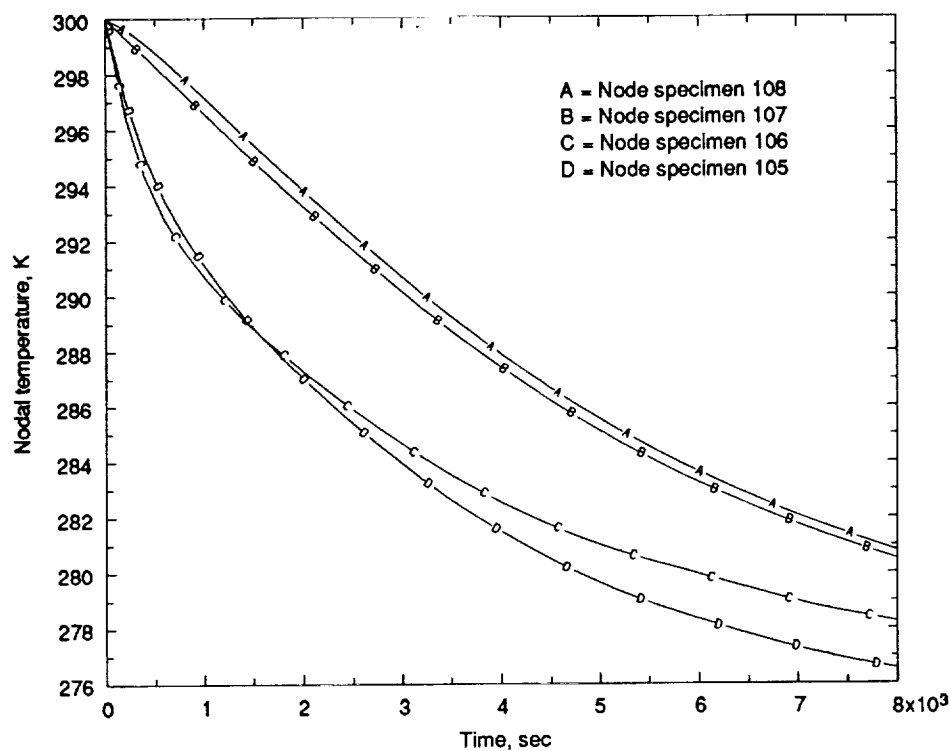


(a) Initial heatup scenario.

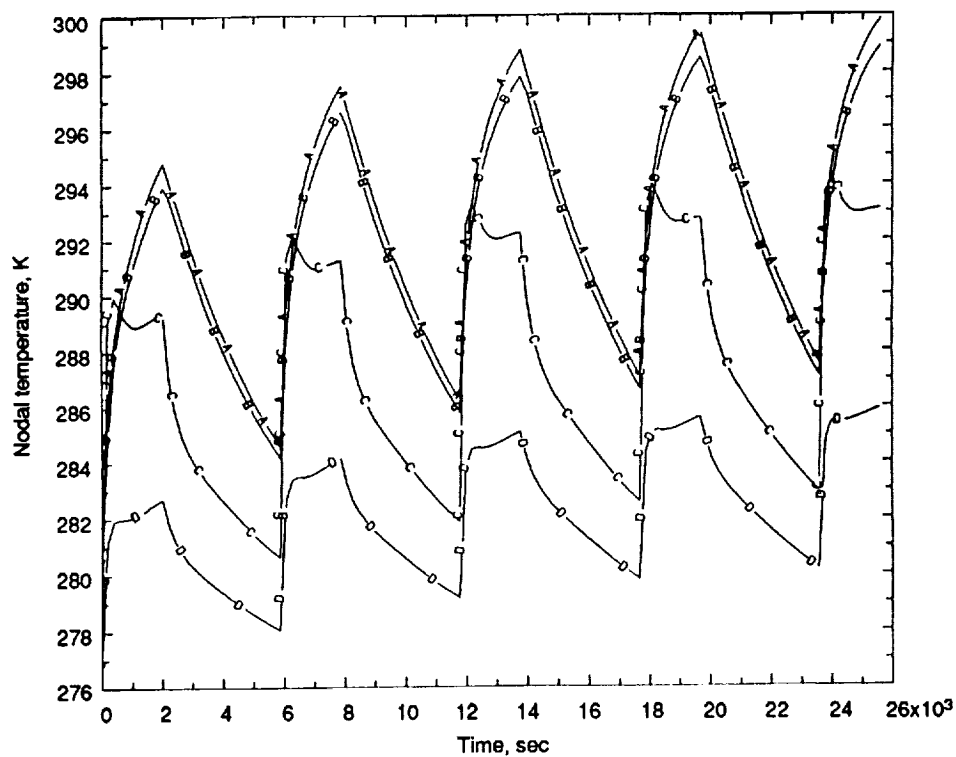


(b) Freeze/melt cycle scenario.

Figure B12.—Conductor-rod nodes at inner radius.

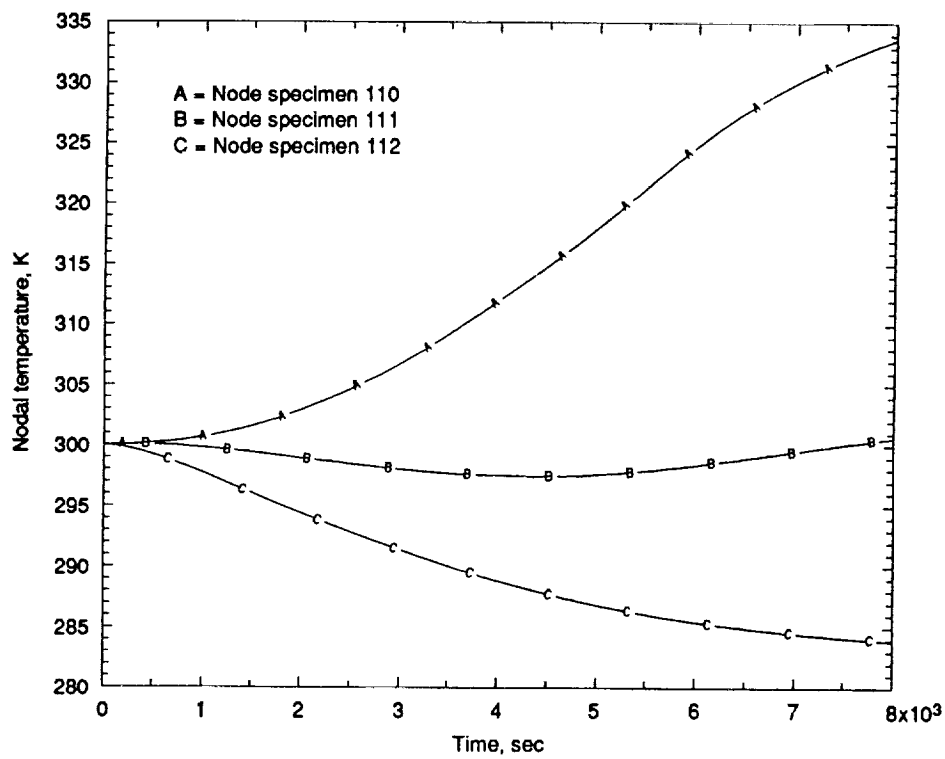


(a) Initial heatup scenario.

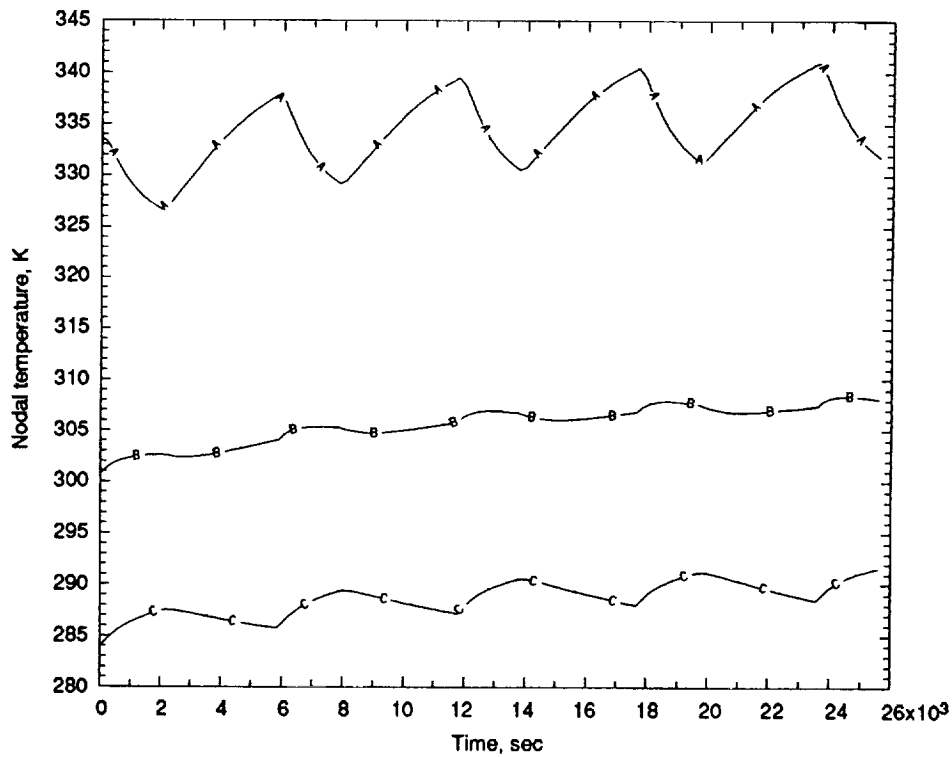


(b) Freeze/melt cycle scenario.

Figure B13.—Lid and GAS wall nodes.

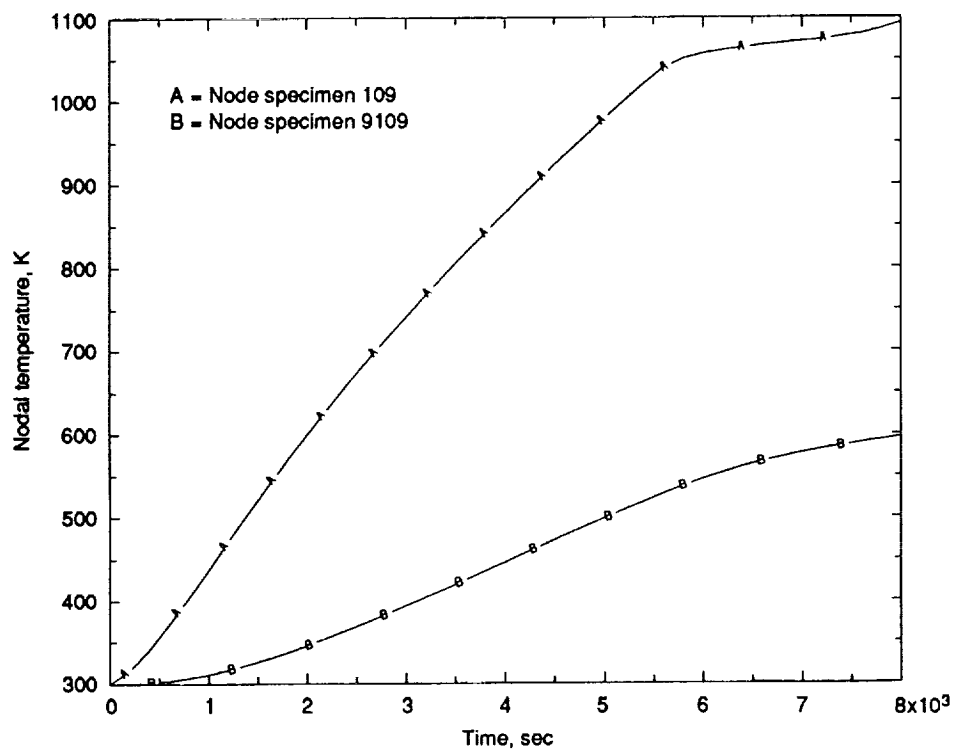


(a) Initial heatup scenario.

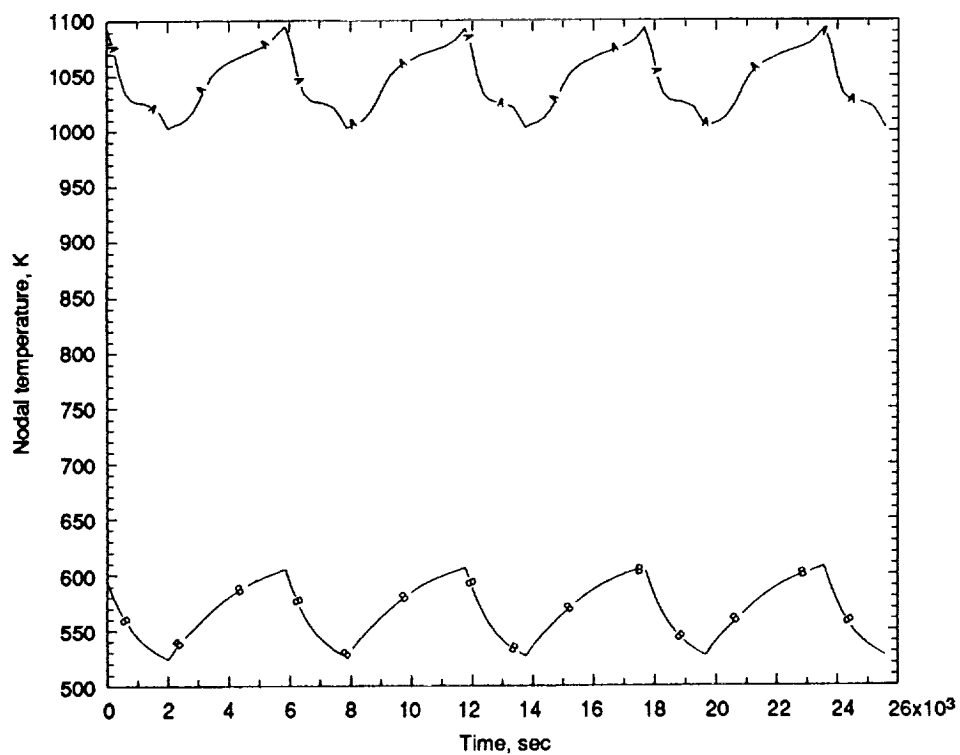


(b) Freeze/melt cycle scenario.

Figure B14.—Mounting-base nodes.

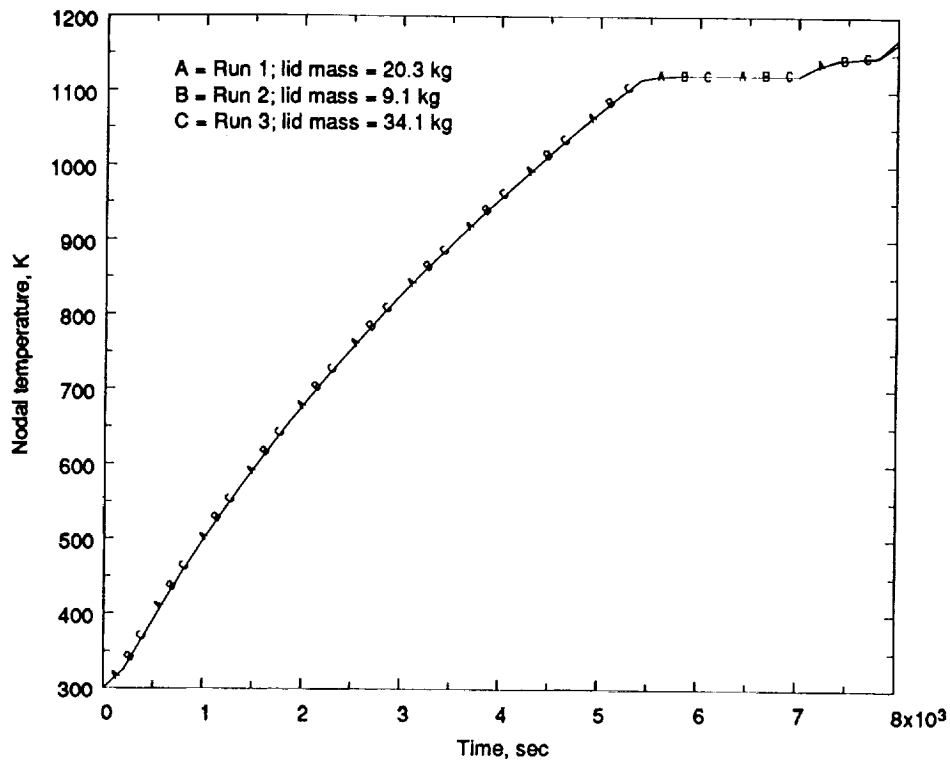


(a) Initial heatup scenario.

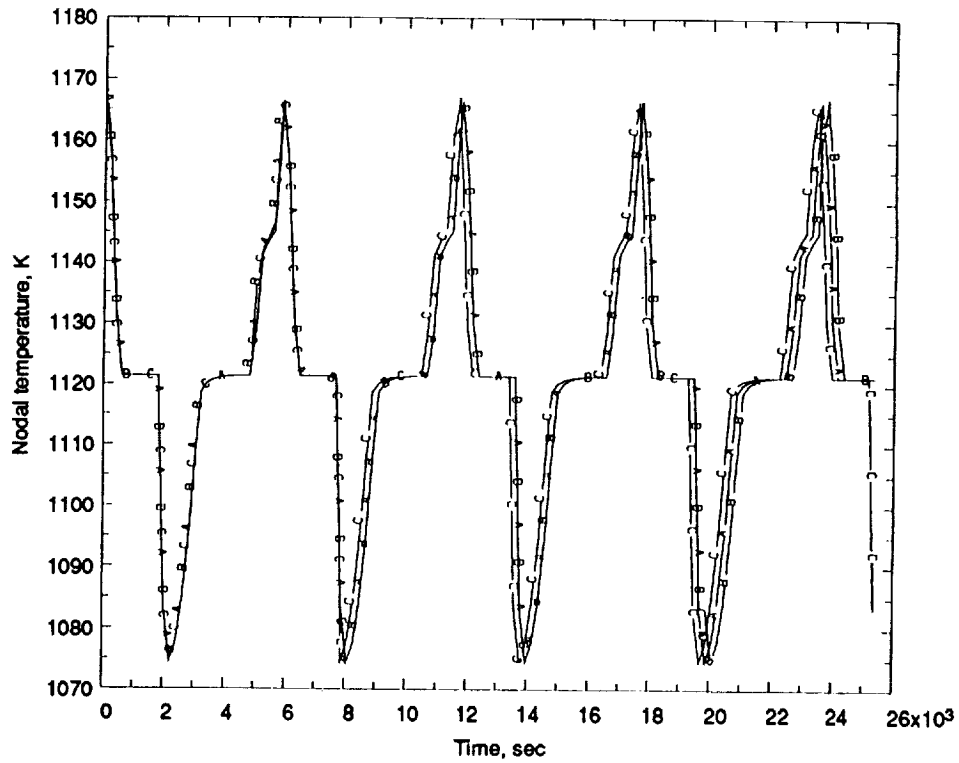


(b) Freeze/melt cycle scenario.

Figure B15.—Spacer nodes.

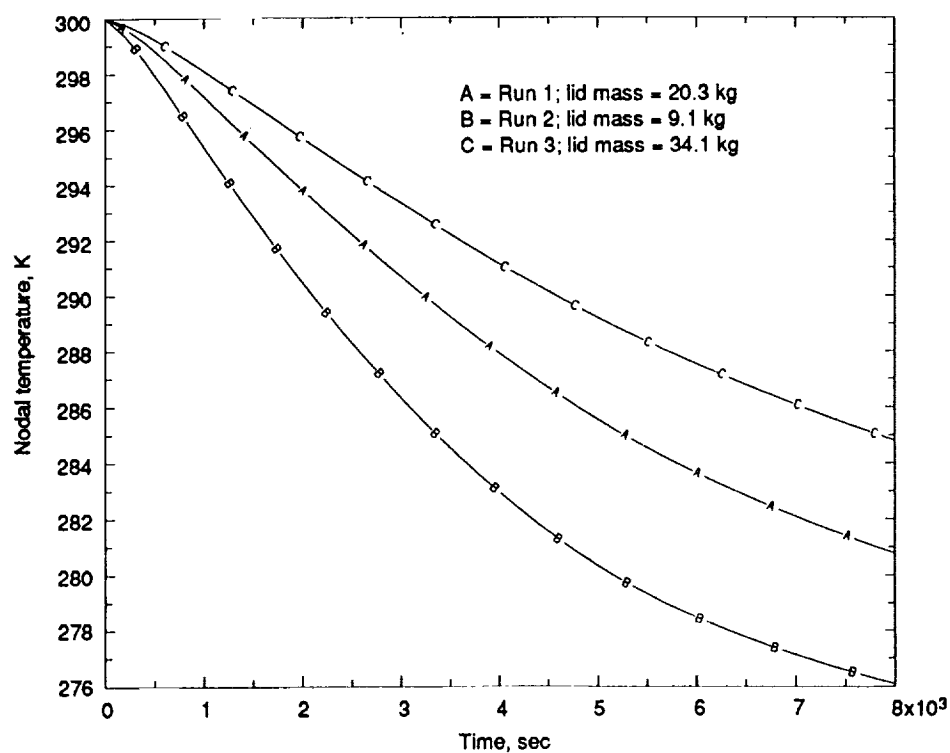


(a) Initial heatup scenario.

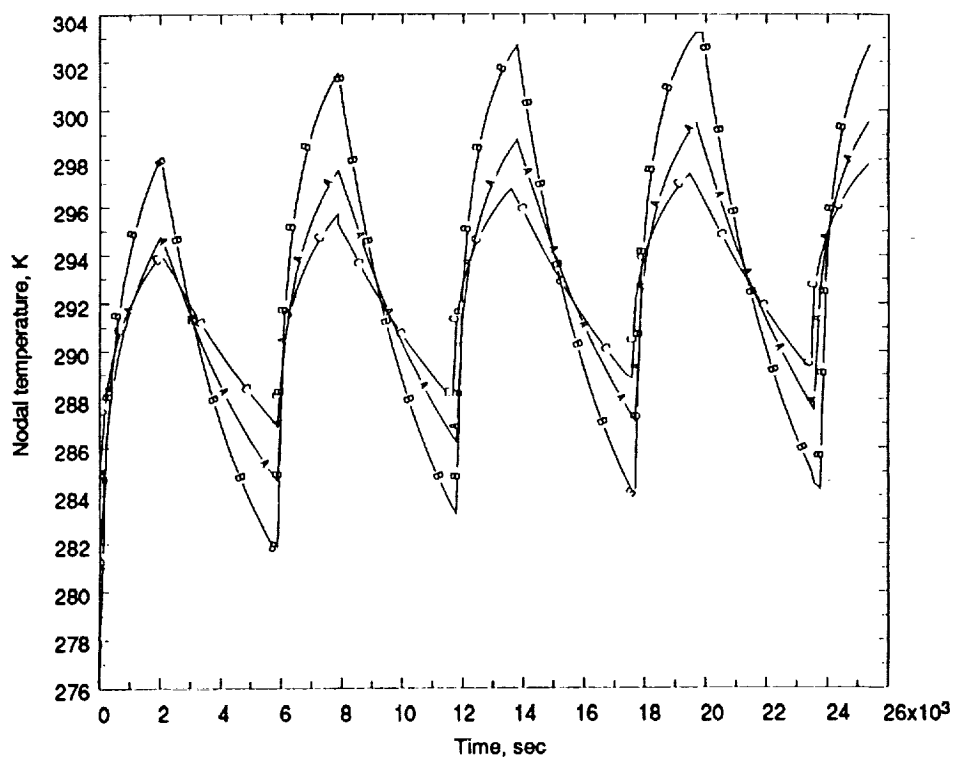


(b) Freeze/melt cycle scenario.

Figure B16.—Effect of lid mass on PCM temperature for PCM node 46.



(a) Initial heatup scenario.



(b) Freeze/melt cycle scenario.

Figure B17.—Effect of lid mass on lid temperature for lid node 108.

Appendix C

Temperature Contour Plots

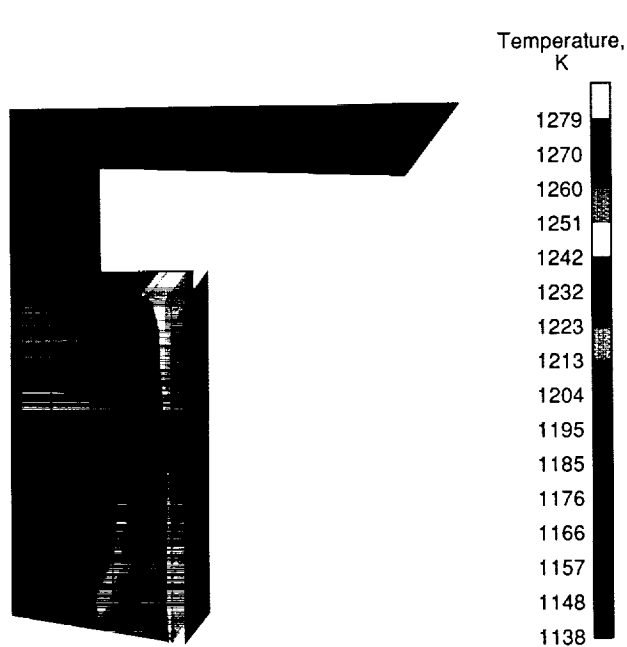


Figure C1.—Run 1 temperature contours of TES specimen after initial heatup. Heater power, 260 W; environmental (sink) temperature, 250 K.

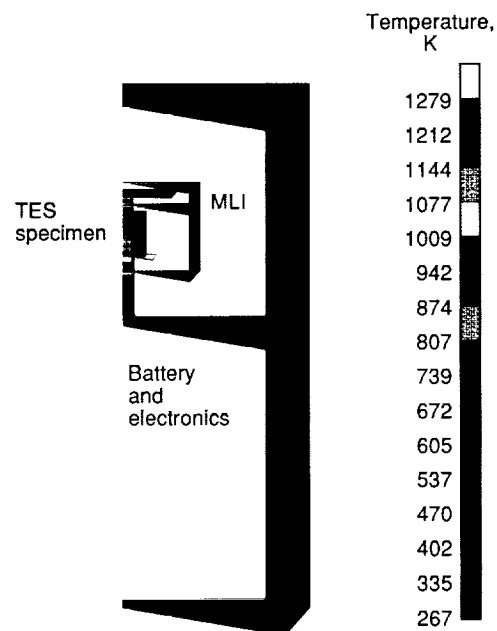


Figure C3.—Run 1 temperature contours of overall TES/GAS configuration after initial heatup. Heater power, 260 W; environmental (sink) temperature, 250 K.

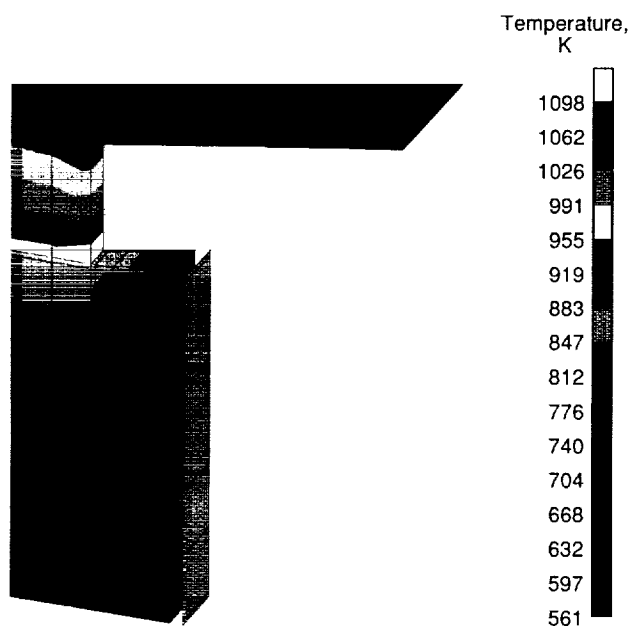


Figure C2.—Run 1 temperature contours of TES specimen after cycle-5 solidification. Heater power, 260 W; environmental (sink) temperature, 250 K.

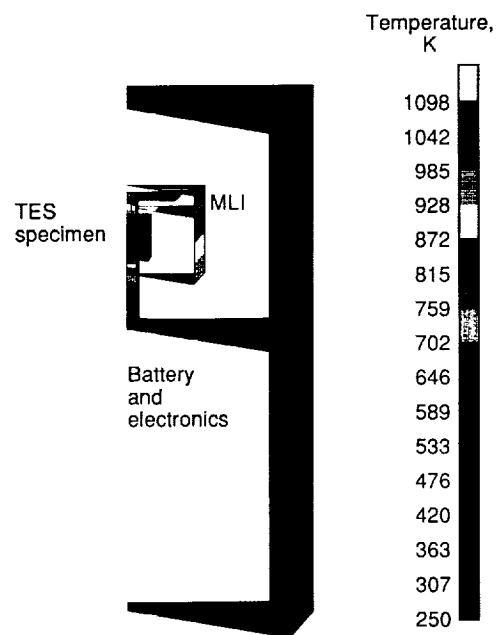


Figure C4.—Run 1 temperature contours of overall TES/GAS configuration after cycle-5 solidification. Heater power, 260 W; environmental (sink) temperature, 250 K.

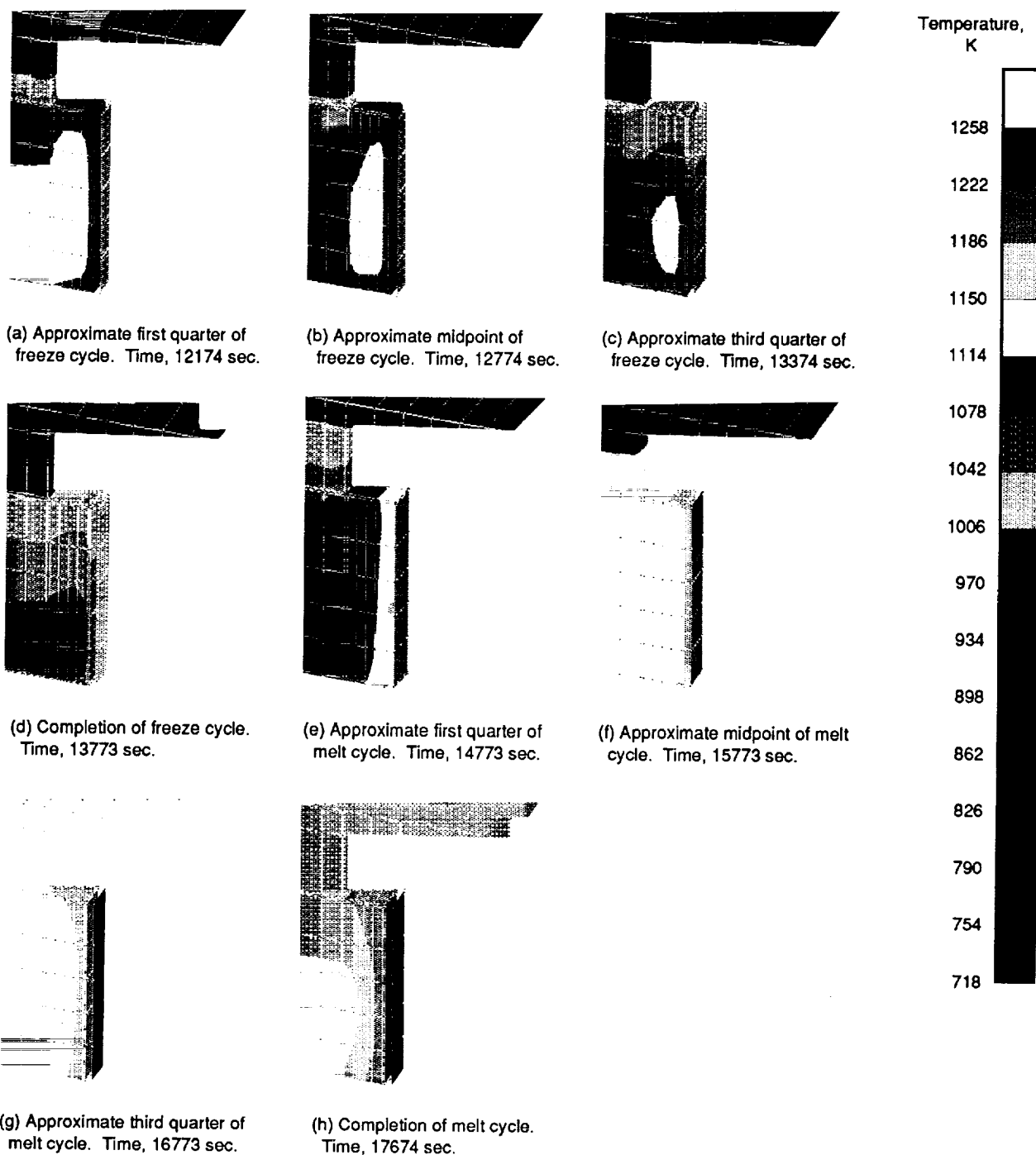


Figure C5.—Run 1 temperature contours of TES specimen during cycle 3.

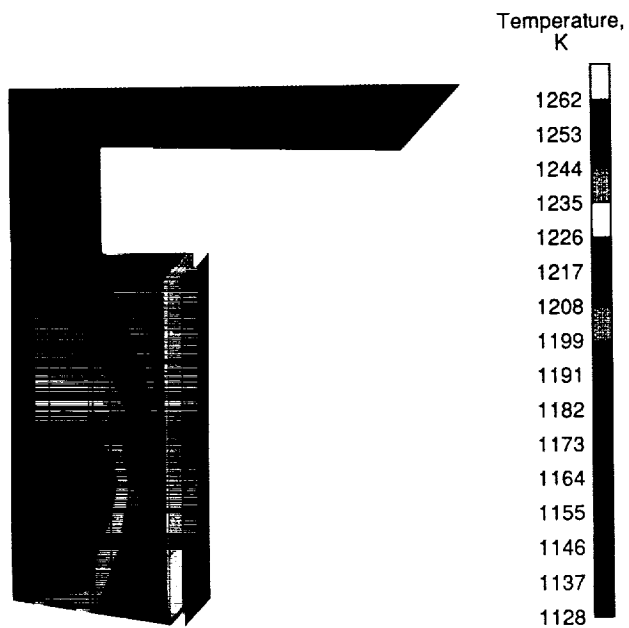


Figure C6.—Run 4 temperature contours of TES specimen after initial heatup. Heater power, 260 W; environmental (sink) temperature, 250 K.

ORIGINAL PAGE
COLOR PHOTOGRAPH

References

1. Namkoong, D.: Flight Experiment of Thermal Energy Storage. NASA TM-102081, 1989.
2. Kerslake, T.W.; and Ibrahim, M.B.: Analysis of Thermal Energy Storage Material With Change-of-Phase Volumetric Effects. NASA TM-102457, 1990.
3. Wichner, R.P., et al.: Thermal Analysis of Heat Storage Canisters for a Solar Dynamic, Space Power System. ORNL/TM-10665, Oak Ridge National Lab., 1988.
4. Drake, J.B.: Modeling Convective Marangoni Flows with Void Movement in the Presence of Solid-Liquid Phase Change. ORNL-6516, Oak Ridge National Lab., Jan. 1990.
5. Holman, J.P.: Heat Transfer. 5th ed., McGraw-Hill, 1981.
6. Rohsenow, W.M.; Hartnett, J.P.; and Ganic, E.N., eds.: Handbook of Heat Transfer Fundamentals. 2nd Ed., McGraw-Hill, 1985.
7. Lunardini, V.J.: Heat Transfer In Cold Climates. Van Nostrand Reinhold Company, 1981.
8. Williams, P.T.: Thermal Radiative Transport Through LiF For Temperatures Near The Melting Point. K/CSD/TM-77, Oak Ridge National Lab., Feb. 1988.

REPORT DOCUMENTATION PAGE			Form Approved OMB No. 0704-0188	
Public reporting burden for this collection of information is estimated to average 1 hour per response, including the time for reviewing instructions, searching existing data sources, gathering and maintaining the data needed, and completing and reviewing the collection of information. Send comments regarding this burden estimate or any other aspect of this collection of information, including suggestions for reducing this burden, to Washington Headquarters Services, Directorate for Information Operations and Reports, 1215 Jefferson Davis Highway, Suite 1204, Arlington, VA 22202-4302, and to the Office of Management and Budget, Paperwork Reduction Project (0704-0188), Washington, DC 20503.				
1. AGENCY USE ONLY (Leave blank)		2. REPORT DATE November 1991	3. REPORT TYPE AND DATES COVERED Technical Memorandum	
4. TITLE AND SUBTITLE Thermal Modeling With Solid/Liquid Phase Change of the Thermal Energy Storage Experiment			5. FUNDING NUMBERS WU-506-41-31	
6. AUTHOR(S) J. Raymond Lee Skarda				
7. PERFORMING ORGANIZATION NAME(S) AND ADDRESS(ES) National Aeronautics and Space Administration Lewis Research Center Cleveland, Ohio 44135-3191			8. PERFORMING ORGANIZATION REPORT NUMBER E-6032	
9. SPONSORING/MONITORING AGENCY NAMES(S) AND ADDRESS(ES) National Aeronautics and Space Administration Washington, D.C. 20546-0001			10. SPONSORING/MONITORING AGENCY REPORT NUMBER NASA TM-103770	
11. SUPPLEMENTARY NOTES Responsible person, J. Raymond Lee Skarda, (216) 433-8728.				
12a. DISTRIBUTION/AVAILABILITY STATEMENT Unclassified - Unlimited Subject Category 34			12b. DISTRIBUTION CODE	
13. ABSTRACT (Maximum 200 words) A thermal model which simulates combined conduction and phase change characteristics of thermal energy storage (TES) material is presented. Both the model and results are provided herein for the purpose of benchmarking the conduction and phase change capabilities of recently developed and unvalidated microgravity TES computer programs. The model was originally developed to support the design and analysis of the NASA Lewis Research Center TES experiment. This report also serves as the preliminary documentation of the thermal models constructed for this experimental effort. The phase change approach developed for the model can be applied to most commercial thermal analyzers and also can be used for other phase change applications. It is again emphasized that the principal intent of this report is to present a model and results for evaluating (benchmarking) computer codes that have been recently developed to predict the behavior of phase change materials in a microgravity environment. Specifically, operation of the TES-1 experiment is simulated. The heart of the TES-1 experiment is the TES specimen. The specimen is mounted in an approved shuttle payload container known as a Get-Away-Special (GAS), which is also included in the model. The TES specimen consists of the torus shaped TES canister which contains the phase change material (PCM), the conductor rod, and the radiator flare. A heater radiates heat to the outer radius of the TES canister during melting of the PCM. After the lithium fluoride PCM is completely melted, the heater is turned off and latent heat is transferred from the PCM to the conductor rod at the TES canister inner radius. The removed heat is radiated to the environment from the TES radiator flare during solidification. A series of five melting/freezing cycles are simulated. A two-dimensional SINDA85 model of the TES experiment in cylindrical coordinates was constructed. The phase change model accounts for latent heat stored in, or released from, a node undergoing melting and freezing. However, the volume change of the LiF during the phase change process is neglected. Other phenomena not considered in the model include buoyancy driven and Marangoni flows and the semitransparent behavior of the lithium fluoride (LiF). Three types of results provided for comparison with other models are transient temperature profiles, color temperature contour plots, and tabulated results. Tabulated results are peak temperatures, freezing times, melting times, and heat losses following each freeze and thaw period. Results from four simulations are presented. Three simulations were performed to investigate the effects of the GAS lid mass on the melting and freezing times of the PCM. The fourth simulation uses a simple approximation to account for combined radiation and conduction transport through the liquid LiF (the semitransparent nature of the solid phase was not included). Results from the lid mass comparison indicate negligible effect on the freezing and melting times for GAS lid masses from 9.1 to 34.1 kg. The semitransparent approximation resulted in decreases of 3.9 percent in freezing times, 3.8 percent in melting times, and 20 K in peak canister temperatures with respect to conduction only.				
14. SUBJECT TERMS Phase change Thermal energy storage Thermal modeling			15. NUMBER OF PAGES 49	
			16. PRICE CODE A-3	
17. SECURITY CLASSIFICATION OF REPORT Unclassified	18. SECURITY CLASSIFICATION OF THIS PAGE Unclassified	19. SECURITY CLASSIFICATION OF ABSTRACT Unclassified	20. LIMITATION OF ABSTRACT	

